Department of Physics and Astronomy
University of Heidelberg

Bachelor Thesis in Physics
submitted by

Yannis Seemann

born in Hamm (Germany)

2019

Production of (anti-)deuterons in Pb-Pb collisions and via the spallation process

This Bachelor Thesis has been carried out by Yannis Seemann at the
Physics Institute in Heidelberg
under the supervision of
Prof. Dr. Silvia Masciocchi

Abstract

Understanding the production processes for particles in heavy-ion collisions plays a key role within the ALICE experiment. However, in order to study and understand the production of particles, all sources of particles need to be taken into account. In this thesis, one source will be investigated in detail, namely the spallation process, which is responsible for particle production in the detector material and forms a background contribution to particles produced in the initial collision. In particular, this thesis is focused on deuteron production within this process in Pb-Pb collisions at $\sqrt{s_{\mathrm{NN}}} = 5.02\,\mathrm{TeV}$. In the course of this thesis, new discrimination criteria to distinguish deuterons from spallation and deuterons originating from the primary collision will be examined and the resolution of anti-deuterons will be studied. Lastly, the fraction of primary deuterons will be determined using a fitting method. This fitting method will also be improved in this context.

Zusammenfassung

Dem Verständnis der Produktionsprozesse für Teilchen in Schwerionenkollisionen kommt eine herausragende Bedeutung im Programm des ALICE Experiments zu. Allerdings müssen für das Verständnis und die Analyse der Produktion von Teilchen alle möglichen Quellen in Betracht gezogen werden. In dieser Arbeit wird eine der Quellen, nämlich der Spallation-Prozess, genauer untersucht. Dieser beschreibt die Teilchenproduktion im Material der Detektoren, die, neben der Produktion von Teilchen in der initialen Kollision, einen Beitrag zu allen gemessenen Teilchen liefert. Diese Arbeit behandelt insbesondere die Produktion von Deuteronen im Zuge des Spallation-Prozesses in Pb-Pb Kollisionen bei einer Schwerpunktsenergie von $\sqrt{s_{\mathrm{NN}}} = 5.02\,\mathrm{TeV}$. Im Laufe dieser Arbeit werden Kriterien zur besseren Unterscheidbarkeit von aus dem Spallation-Prozess und aus der primären Kollision stammenden Deuteronen herausgearbeitet, die Auflösung von Anti-Deuteronen wird systematisch untersucht und der Anteil der primären Deuteronen wird unter Verwendung einer Fit-Prozedur bestimmt. Im Rahmen des letzten Punkts wird zudem die Fit-Prozedur verbessert.

Contents

1. Introduction **1**

2. Particle production in heavy-ion collisions **3**

2.1. Event characterization 3

2.1.1. Centrality 4

2.2. Space time evolution of the collision 5

2.3. Particle production process 6

2.3.1. Spallation Process 7

2.3.2. The Statistical Hadronization and the Coalescence model 9

3. ALICE experiment **13**

3.1. The ALICE coordinate system and the pseudorapidity 14

3.2. The Inner Tracking System 15

3.3. The Time Projection Chamber 15

3.4. The Time Of Flight detector 16

3.5. Event reconstruction 16

3.6. Particle identification 18

3.6.1. ITS and TPC particle identification 18

3.6.2. TOF particle identification 20

3.7. Monte Carlo simulations 21

4. Deuteron selection and discrimination criteria **23**

4.1. Data 23

4.2. Deuteron selection 24

4.3. Separation of primary and secondary deuterons 27

4.4. Secondary deuteron selection 28

4.5. Possible new criteria for primary deuteron selection 29

4.5.1. ITS hits 29

4.5.2. Shared clusters in the ITS 30

4.5.3. dE/dx-Eta distribution 32

4.5.4. Chi2/NDF-distributions for ITS and TPC 33

5. DCA resolution of anti-deuterons **35**
5.1. Data 35
5.2. Resolution 36
5.3. DCA resolution for different ITS requirements 37
5.4. Centrality dependency of the resolution 40

6. Fraction of primary deuterons **43**
6.1. Fitting procedure 43
6.2. Fraction of primary deuterons as a function of multiplicity 48
6.3. Fitting procedure with decay deuterons 49
6.4. 2D-fit 52

7. Summary and outlook **55**

Bibliography **ix**

A. Additional results **xi**

1. Introduction

This thesis is in general embedded in the studies of the production of nuclei in hadronic interactions. Special emphasis is laid in this context on the production of anti-deuterons and deuterons in ALICE in Pb-Pb collisions at a center of mass energy of $\sqrt{s_{\mathrm{NN}}} = 5.02\,\mathrm{TeV}$. In order to analyze and understand the production of (anti-)particles, all sources of these particles need to be considered, since only the sum of the different contributions is measured within the experiment. In general, two groups of particles can be identified. On the one hand, particles can be produced in the initial collision of lead nuclei at the so-called primary vertex. These particles are referred to as primary particles. The production processes for primary particles are not yet fully understood. However, two different, competing models are proposed to describe the processes, namely the statistical hadronization model [1] and the coalescence model [2], which will be outlined briefly within this thesis. On the other hand, there are the so-called secondary particles, which do not originate from the primary vertex but are produced in secondary interactions. These secondary particles can essentially be categorized into two classes, characterized by their underlying production process, which are rather well understood. The first class consists of (anti-) particles that are produced in weak decay processes of heavier (anti-)particles, in the case of (anti-)deuterons the driving process is the decay of the (anti-)hyper-triton ($^{3}_{\Lambda}\bar{\mathrm{H}} \longrightarrow \bar{\mathrm{d}} + \bar{\mathrm{p}}(\mathrm{n}) + \pi^{+}(\pi^{0})$, $^{3}_{\Lambda}\mathrm{H} \longrightarrow \mathrm{d} + \mathrm{p}(\mathrm{n}) + \pi^{-}(\pi^{0})$) which produces (anti-)deuterons. The second class consists of particles, that are produced in the detector material for example via the so-called *spallation process*. In this process, primary particles of all species interact with the detector material and secondary particles are emitted by spallation, among which are also light nuclei up to a mass number of 4 like deuterons. Only particles (excluding anti-particles) can be produced within this process since the secondary particles that are emitted, are fragments of former nuclei which do not contain anti-matter. Furthermore, the production of anti-nuclei is suppressed by the baryon number conservation, meaning every time an anti-nucleus is formed also a nucleus needs to be produced, which takes a lot of energy and is therefore unlikely. Secondary particles produced in spallation are characterized by a relatively flat angular distribution in contrast to the primary particles, which are pointing directly to the primary vertex. This will be taken advantage of in the course of this thesis. A detailed description of the exact production process will be given in chapter 2. The characterization and selection of nuclei produced via spallation will be the main subject of investigation in this thesis, a detailed description of the properties of spallation leads to a better understanding of this production mechanism and is essential for the understanding of the other production processes. This thesis is dedicated

to the discrimination between primary and secondary deuterons and the examination of spallation properties. Concerning these topics, three major parts arise that will be studied in detail:

1. **Discrimination between primary and secondary deuterons**
   The first goal of this thesis is to achieve better discrimination between primary and secondary deuterons. The most prominent variable hitherto is the Distance of Closest Approach (DCA), which quantifies the shortest distance between the primary vertex and the particle's track. It is commonly projected into the DCA in the transverse plane with respect to the beam (DCA_{xy}) and the DCA in the longitudinal direction of the beam (DCA_{z}). If a particle originates directly from the primary vertex, its DCA value is zero within a certain resolution. This resolution is limited due to the uncertainties of the reconstructed track of the particle as well as the uncertainties of the position of the primary interaction vertex. These uncertainties are mainly dependent on the intrinsic detector resolution which is influenced by several factors, including the granularity of the detectors. This is also the reason why the resolution on the DCA_{z} is worse than on the DCA_{xy}. Depending on the curvature of the tracks, the DCA has a positive value (vertex inside the curvature) or a negative one (vertex outside the curvature). Secondary deuterons do not originate from the primary vertex but are mostly produced by spallation in the detector material. Therefore, when their tracks are propagated to the vertex, their DCA results mostly non-zero. This leads to different shapes in the DCA distributions of primary and secondary particles, which can be used for distinguishing them. However, this variable is not able to fully discriminate primary and secondary particles, therefore other variables, that might be useful for the discrimination will be investigated in this part.

2. **DCA resolution studies of (anti-)deuterons**
   The second part is dedicated to the study of the DCA resolution of primary deuterons. Resolution refers in this case to the width of the DCA distribution of primary particles, which is influenced by the track and primary vertex uncertainties. In the context of this part, the resolution will be studied for various detector requirements as well as for different collision systems and for Monte Carlo simulations. This will be done to verify the Monte Carlo simulation as well as preparing the fitting procedure used in chapter 6.

3. **Fraction of primary (anti-)deuterons**
   The third part is dedicated to the determination of the fraction of primary particles in relation to all produced particles. This is especially important if yields of particles in the collisions are measured since secondary particles form a background contribution. To determine the fraction of primary particles, a fitting procedure using Monte Carlo simulations will be introduced. Furthermore, improvements to the fitting procedure will be outlined and discussed in the course of this work.

2. Particle production in heavy-ion collisions

In this chapter a short overview of the collision geometry and the space-time evolution of heavy-ion collisions will be given, as well as different approaches modeling particle production in ultra-relativistic heavy-ion collisions. This is of particular importance to understand the production processes and forms the basis for the upcoming analysis.

2.1. Event characterization

In order to describe an event of the collision of two nuclei, geometrical considerations are taken into account. The most important characteristic of the collision is how centrally the nuclei collide since this defines the number of particles, that are produced in the collision. This can be characterized by the impact parameter vector $\vec{b}$, which connects the centers of the colliding nuclei in the plane transverse to the beam, as it is depicted in Figure 2.1. If the impact parameter $\vec{b}$ is zero, the two nuclei collide most centrally, if it is about the diameter of the nuclei, the two nuclei barely interact via the strong force. This impact parameter $\vec{b}$ cannot be measured directly, since it is within the magnitude of an atomic nucleus, approximately a few femtometers. But because it is correlated to the multiplicity (number of particles produced in the collision), which can be measured, the impact parameter can be determined by applying phenomenological or geometrical models. This leads to the definition of the centrality, discussed in subsection 2.1.1.

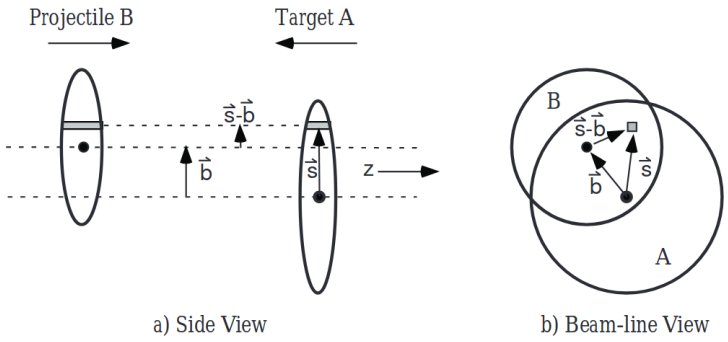

Figure 2.1.: Schematic representation of the collision between nuclei with impact parameter $\vec{b}$. Nuclei are elliptical in the side view because of Lorentz contraction. Taken from [3].

2.1.1. Centrality

This description is based on [4] and [5]. The centrality of an event is simply speaking a parameter describing the overlap of the two nuclei in the collision, which is directly connected to the impact parameter $\vec{b}$. It ranges from 0% to 100%, where 0% is the most central with an impact parameter $\vec{b} = 0$ (high multiplicity) and 100% is the most peripheral (low multiplicity), where the colliding particles barely interact via the strong force with each other and the impact parameter is large. In ALICE, it is defined as the percentile of the total hadronic interaction cross-section σ_{AA} of the colliding nuclei, given by

$$c(b) = \frac{\int_0^b \frac{\mathrm{d}\sigma}{\mathrm{d}b'}\mathrm{d}b'}{\int_0^\infty \frac{\mathrm{d}\sigma'}{\mathrm{d}b'}\mathrm{d}b'} = \frac{1}{\sigma_{\mathrm{AA}}}\int_0^b \frac{\mathrm{d}\sigma}{\mathrm{d}b'}\mathrm{d}b'. \tag{2.1}$$

Taking into account the assumption, that, on average, the particle multiplicity at mid rapidity increases monotonically with the overlap region, the centrality can be written as

$$c \approx \frac{1}{\sigma_{\mathrm{AA}}}\int_{N_{\mathrm{ch}}}^\infty \frac{\mathrm{d}\sigma}{\mathrm{d}N'_{\mathrm{ch}}}\mathrm{d}N'_{\mathrm{ch}} \tag{2.2}$$

and the cross-section may be replaced with the number of observed events N_{ev}, corrected for the trigger efficiency, which describes the limited efficiency of the trigger detectors to detect particles, and for the non-hadronic interaction background, which for example occurs when particles coming from outside traverse the detectors:

$$c \approx \frac{1}{N_{\mathrm{ev}}}\int_{N_{\mathrm{Ch}}}^\infty \frac{\mathrm{d}n}{\mathrm{d}N'_{\mathrm{ch}}}\mathrm{d}N'_{\mathrm{ch}}. \tag{2.3}$$

In the experiment, the detector which is mainly used for centrality determination is the V0 detector. It is a detector, that consists of two arrays (V0A and V0C) with scintillator counters installed on either side of the interaction point, which measure the energy deposit of the traversing particles and provide time information about the collision. To determine the centrality, the energy deposited in the two disks of the detector is summed up into the amplitude. The distribution of the amplitude of the V0 detector is then fitted with a parametrization based on the Glauber Monte Carlo model [6] and the Negative Binomial Distribution (NBD-Glauber fit). The centrality classes are then calculated by integrating the events, as shown in Figure 2.2.

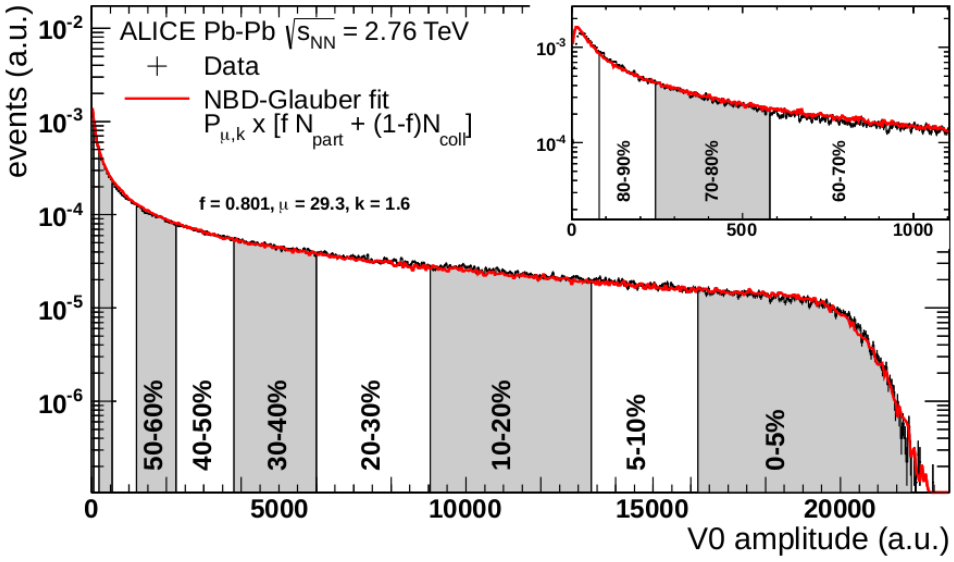

Figure 2.2.: Example of NBD-Glauber fit to the distribution of V0 amplitude (sum of V0A and V0C). Centrality bins are defined by integration, the most peripheral region is depicted in the upper right corner [4].

2.2. Space time evolution of the collision

To get an understanding of the different approaches to describe particle production one has to clarify the evolution of the system of two colliding heavy nuclei and its properties. The collision process is illustrated in the space-time diagram of Figure 2.3. This section is based on information from [7].

1. $t < 0$ $\frac{\text{fm}}{\text{c}}$: The two Lorentz contracted nuclei approach each other along the z-axis (beam-line).
2. $t = 0$ $\frac{\text{fm}}{\text{c}}$: Time of collision. In the first approximation, the geometry can be described with the Glauber model.
3. $0 < t <\sim 1$ $\frac{\text{fm}}{\text{c}}$: Pre-equilibrium, at first instance hard processes with high transferred momentum occur between the partons and particles with high energy (mass or momentum) are produced. Partons undergo several interactions, a hot dense medium is produced. This phase in not well understood yet.
4. $1 \lesssim t \lesssim 10$ $\frac{\text{fm}}{\text{c}}$: Local equilibrium is established, a Quark-Gluon Plasma phase is formed if the temperature T of the system is above the critical temperature T_{C} which defines the boundary to the QGP phase, and the system is expanding rapidly, while it is cooling down.
5. $10 \lesssim t \lesssim 15$ $\frac{\text{fm}}{\text{c}}$: When the phase boundary is reached ($T \simeq 160\,\text{MeV}$), the hadronization starts and the quarks bind together. The system has evolved into an interacting hadron resonance gas. When inelastic interactions between the particles cease due to not sufficiently

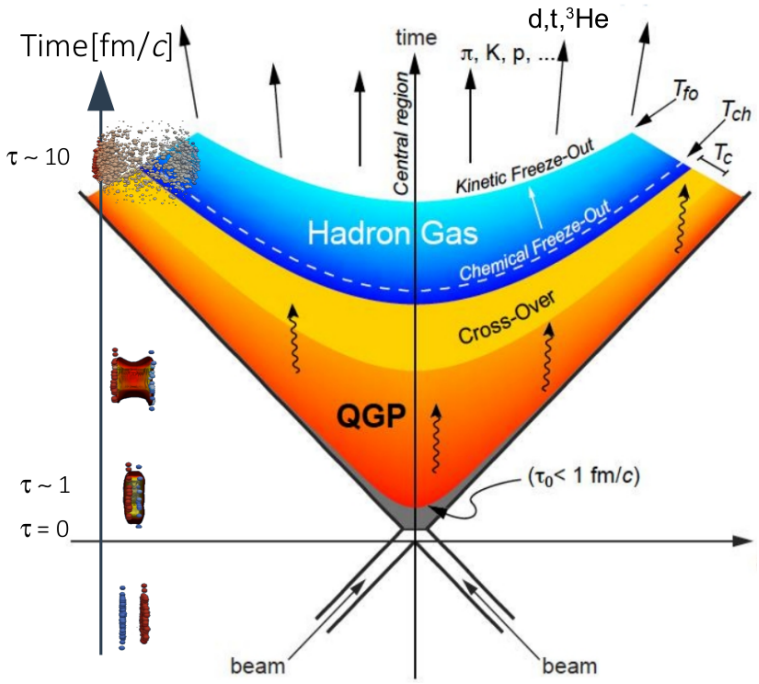

Figure 2.3.: Space time diagram for the evolution of a heavy-ion collision. Taken from [7].

large momentum exchanges between the hadrons, the chemical composition of the system is fixed. This is called the *chemical freeze-out* and at this point, particle yields up to resonance decays are fixed. The temperature at this point is approximately $T_{\mathrm{chem}} \sim 156\,\mathrm{MeV}$ [1] for the LHC. At a temperature of $T_{\mathrm{kin}} \sim 100\,\mathrm{MeV}$ also elastic reactions cease at the *kinetic freeze-out*, after this the particles spectra and correlations are frozen.

In the experiment, only the sum of all interactions in all phases can be measured. Therefore, theoretical models can be applied to disentangle the production processes and characterize each phase.

2.3. Particle production process

When it comes to particle production in hadronic collisions, three different production processes have to be considered. At first, the particle production in the primary interaction in the collision, which contributes the most to produced particles and is commonly the main subject of investigation in heavy-ion collisions. Secondly, the process of spallation, which describes particle production in the detector and which will be the main subject of investigation in this thesis, and third, the production via decay processes of heavier particles. In the following, the spallation process, as it is crucial for this thesis will be described in detail, whereas two major model classes for particle production in the primary collision, namely Statistical Hadronization Models and the Coalescence

Model, will be outlined briefly. This will be done, since especially when considering the production of light (anti-)nuclei in heavy-ion collisions the question arises, how these loosely bound objects (e.g. binding energy of deuterons: 2.2 MeV) can form and survive at temperatures reached in the collisions. The decay process will not be described here.

2.3.1. Spallation Process

The spallation process refers to nuclear reactions, in which a light energetic projectile (e.g. proton, neutron, or light nucleus) interacts with an atomic nucleus and causes the emission of a large number of hadrons or fragments [8]. This process is present in various fields like cosmology and astrophysics, cosmic ray physics, planetary and geochemical science, and, last but not least, nuclear physics [9]. The observations of particle cascades in cosmic ray interactions have been done already in the 1930s and accelerator-driven spallation reactions have been discovered in 1947 [8]. However, these processes are not yet fully understood, and especially spallation in the detectors of an experiment like ALICE has been studied little, although it is a key aspect for understanding nuclei production processes. According to current views, spallation can be described by two stages, the intra-nuclear cascade and the deexcitation. The theoretical description of the spallation process in this section mainly follows [8].

1. **Intra-nuclear cascade**
   In the first stage of the process, the incoming projectile interacts with individual nucleons in the target nucleus and loses a large amount of its kinetic energy to these nucleons by elastic collisions. At low projectile energies ($\sim$ 100 MeV), all interactions occur between the nucleons and the process is called nucleon cascade, whereas for higher energies the energy thresholds for particle production are reached. Initially, pions are produced (projectile energy of a few hundred MeV) and with larger energies of 2-10 GeV even heavier hadrons like kaons, protons and deuterons occur. They also contribute and participate in the intra-nuclear cascade and interact with each other, this is called the hadron cascade. Particles with sufficiently large energy to escape from the nucleus are emitted mainly in the direction of the incident particle. The residual energy that was transferred to the nucleons inside the nucleus remains as excitation energy, the nucleons are therefore in a highly excited state. The intra-nuclear cascade is not sharply separated from the equilibrium decay. In a pre-compound state, pre-equilibrium emission can happen, where fast particles or fragments may be emitted after each interaction between the incident or other cascade particles and a nucleon inside the nucleus. Furthermore, especially in heavy-ion collisions, multifragmentation, where many fragments are produced, and break up into individual particles may occur as well.

2. **Deexcitation**

   In the second stage of the process, after the equilibrium was established, the nucleus is in a highly excited state with a small angular momentum and the energy is equally distributed throughout the nucleus. Now evaporation of neutrons or light charged fragments like deuterons, tritons or α-particles with small energies up to $\sim$40 MeV takes place as the nucleon deexcites. The evaporated particles are emitted, in contrast to the first stage, isotropically. When the nucleus does not obtain enough energy to evaporate a neutron (typically below the binding energy of neutrons $\sim$ 8 MeV), it deexcites by γ-emission.

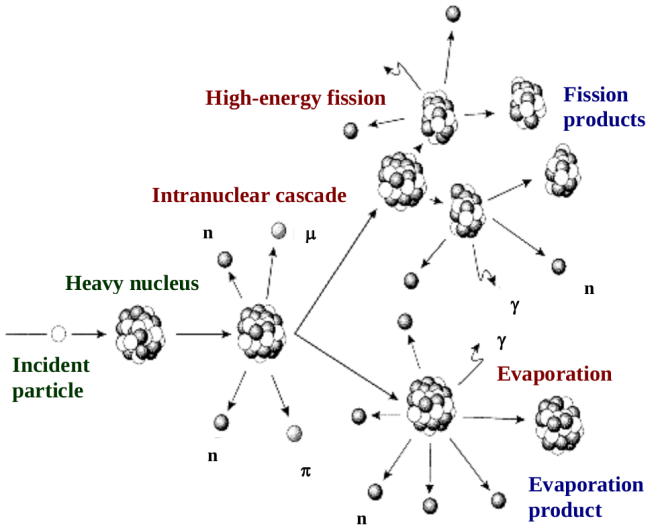

Figure 2.4.: Depiction of the two spallation stages of intra-nuclear cascade and deexcitation. Also given is the competing fission process. Taken from [8].

These spallation processes also take place in ALICE. Here they occur when primary particles, originating from the primary collision, interact with the material of the detectors. As a result, secondary particles with a specific momentum distribution are produced as described above. These particles have an average momentum of about $\sim$1 GeV/c and do not exceed a momentum of 3 GeV/c. Spallation can occur for example in the beam pipe, which is made out of beryllium, in the ITS, which consists of silicon and carbon, and in the containment vessel of the TPC, which is made of composite material. The spallation process is more likely for heavier target nuclei since the interaction cross-section is larger. Directly connected to the production process by spallation is the distribution of the DCA. Because the process leads to more isotropically emitted particles, the DCA distribution is rather flat.

2.3.2. The Statistical Hadronization and the Coalescence model

The hadronization process in the primary interaction of the collision is not yet microscopically understood. However, two alternative, competing mechanisms, namely the Statistical Hadronization model and the Coalescence Model, are proposed. They will be sketched here.

Statistical Hadronization

The statistical hadronization approach is based on thermodynamics. The underlying assumption of this model is, that the system evolves completely statistically under the laws of the Standard Model. In particular, the system of colliding nuclei and the following process of an expanding, thermally equilibrated medium can be modeled using the Grand Canonical Ensemble, which describes an open system (no energy and particle conservation) with the absolute temperature T, the volume V and the chemical potential μ. Within this approach, the Grand Canonical partition function for each particle species is determined, and by superposition of all states, the overall partition function can be obtained. Following this approach, the average number of particles can be expressed as follows [7]:

$$\langle N_i \rangle = \frac{V g_i}{2\pi^2} \int_0^\infty \pm p^2 \ln\left(1 \pm \lambda_i \exp\left(-\beta \epsilon_i\right)\right) dp \tag{2.4}$$

This formula considers the Fermi-Dirac (+) and Bose-Einstein (-) statistics for fermions and bosons, the factor g_i is the number of spin and isospin degenerate states for the specific particle species and ϵ_i is the total energy of one particle with momentum p ($\sqrt{p^2 + m_i^2}$). V is the volume of the system in equilibrium. The chemical potential is given by μ and λ_i is the fugacity, which combines the dependencies of the chemical potentials of the quantum numbers Q (electric charge), S (strangeness) and B (baryon number):

$$\lambda_i\left(T, \mu_i\right) = e^{\beta\left(B_i \mu_B + S_i \mu_S + Q_i \mu_Q\right)} = e^{\beta \mu_i} \tag{2.5}$$

With this approach, the yields of the particles, which are fixed at the chemical freeze-out, can be predicted. This simple statistical approach provides an appropriate description of central collisions in heavy-ion experiments [1], as depicted in Figure 2.5.

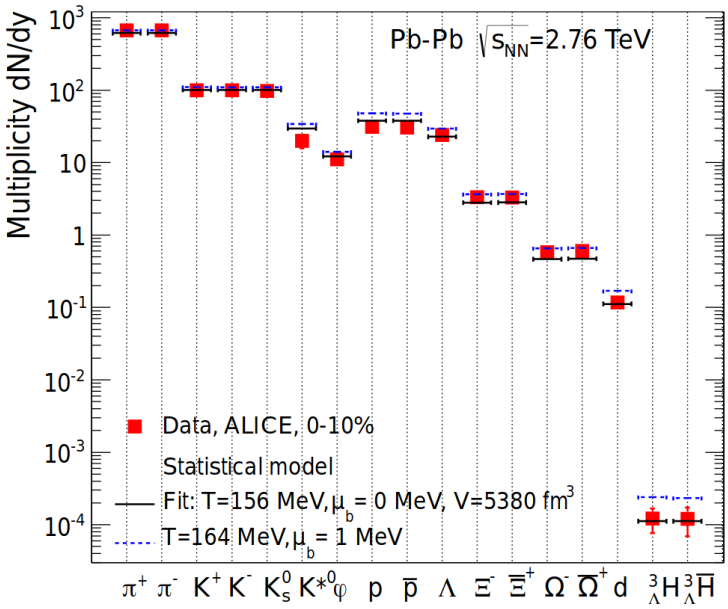

Figure 2.5.: Hadron yields measured by ALICE at the LHC and fit with the statistical hadronization model. Taken from [1].

Coalescence model

Another theoretical approach to the production of light (anti-)nuclei in heavy-ion collisions is the coalescence model. The general idea is, that light nuclei are formed by nucleons at the kinetic freeze-out if they are close enough to each other in phase space (i.e. geometrically and in momentum space) to bind together. Like the Statistical Hadronization Model, this model does not provide any information about the underlying interaction theory and particle production before the kinetic freeze-out.

Within this model, the yield of any nucleus can be calculated by ([7], [2]):

$$\gamma_A \frac{\mathrm{d}^3 N_A}{\mathrm{d}p_A^3} = \frac{2J_A+1}{2^A}\frac{1}{A^3}\left(\frac{4\pi}{3}p_0^3\right)^{A-1}\frac{1}{Z!}\frac{1}{N!}\left(\gamma_\mathrm{p}\frac{\mathrm{d}^3 N_\mathrm{p}}{\mathrm{d}p^3}\right)^Z\left(\gamma_\mathrm{n}\frac{\mathrm{d}^3 N_\mathrm{n}}{\mathrm{d}p^3}\right)^N. \tag{2.6}$$

where A is the nucleon number of the considered particle, Z is the charge number, N is the number of neutrons and $\gamma_A \frac{\mathrm{d}^3 N_i}{\mathrm{d}p_i^3}$ is the relativistic invariant momentum-space density. The first factor characterizes the spin and n (p) refers to neutrons (protons). This equation can be simplified by introducing the coalescence parameter B_A, assuming equal masses of proton and neutron ($m_p = m_n$) and equal p_T spectra. Moreover $\gamma = E/m$ is used.

$$B_A = \frac{2J_A+1}{2^A}\frac{1}{A^3}\frac{1}{Z!}\frac{1}{N!}\left(\frac{4\pi}{3}p_0^3\right)^{A-1}\frac{M_A}{m^A} \tag{2.7}$$

$$E_A \frac{\mathrm{d}^3 N_A}{\mathrm{d}p_A^3} = B_A \left(E_\mathrm{p} \frac{\mathrm{d}^3 N_\mathrm{p}}{\mathrm{d}p_\mathrm{p}^3} \right)^A \tag{2.8}$$

With this formula, the spectra of any light nucleus can be determined using only the parameter B_A and the production spectra of the constituent protons. This simple model can be extended to more sophisticated theories, that take into consideration more realistic assumptions like a p_T dependence of B_A or the system and object size [2].

3. ALICE experiment

A Large Ion Collider Experiment (ALICE) is one of four experiments at the Large Hadron Collider (LHC) at CERN, which focuses on QCD, the strong interaction sector of the Standard Model. It is in particular designed to address the physics of strongly interacting matter at extreme values of energy density and temperature created in nucleus-nucleus collisions, namely the quark-gluon plasma [10].

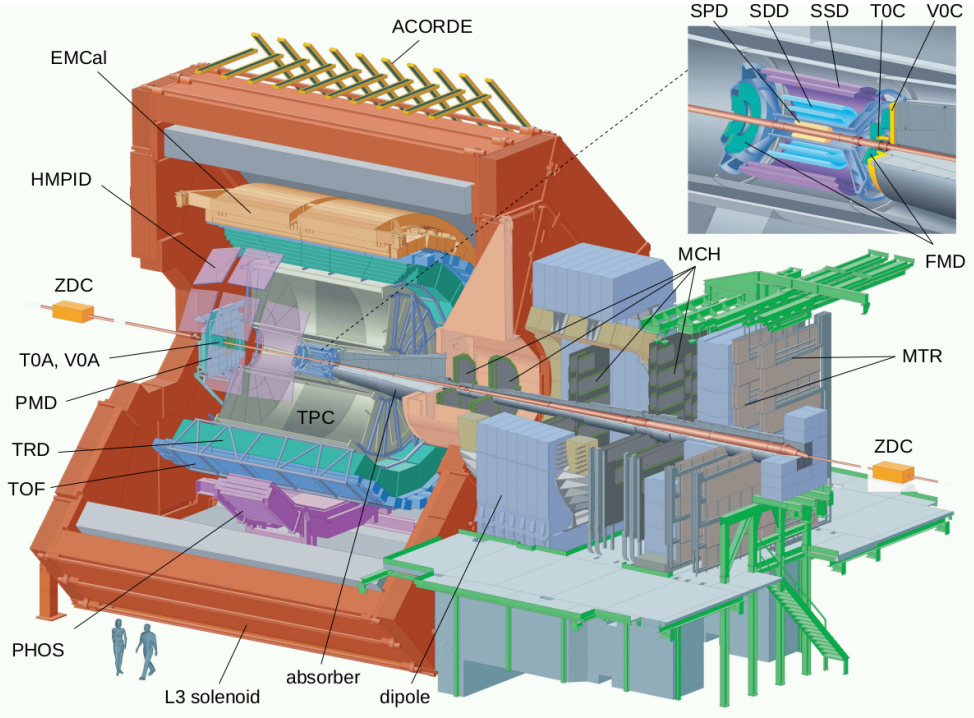

Figure 3.1.: The ALICE detector apparatus at the CERN LHC. The central-barrel detectors (ITS, TPC, TRD, TOF, PHOS, EMCal and HMPID) are embedded in a solenoid with magnetic field $B = 0.5\,\mathrm{T}$. The superstructure of the ITS is delineated in the upper right corner. Taken from [4].

The ALICE apparatus has a total size of $16 \times 16 \times 26\,\mathrm{m}^3$ and weighs approximately 10 000 t [4]. The apparatus and its components are shown in Figure 3.1. It consists of 17 detector systems, which can be divided into three different categories: central-barrel detectors, forward detectors and the MUON spectrometer. In this thesis, the event centrality is determined with the forward detectors, whereas the analysis will be performed using the central barrel detectors. Therefore they will be outlined briefly. The central barrel contains seven detectors, namely the Inner Tracking System (ITS), the Time Projection Chamber (TPC), the Transition Radiation Detector (TRD), the Time

Of Flight (TOF), the Photon Spectrometer (PHOS), the Electromagnetic Calorimeter (EMCal) and the High Momentum Particle Identification Detector (HMPID). These detectors are embedded in the L3 solenoid magnet within a magnetic field of $B = 0.5\,\mathrm{T}$. Because the ITS, TPC and TOF play an important role in this analysis, they will be described in more detail in the following. More details can be found at [10].

3.1. The ALICE coordinate system and the pseudorapidity

To describe the geometry of the detectors, at first the coordinate system as well as the variable of the pseudorapidity have to be clarified. The ALICE coordinate system is a right-handed orthogonal Cartesian system with point of origin $x, y, z = 0$ at the beams interaction point. The axis are defined as follows [11]:

- x-axis: perpendicular to the mean beam direction, aligned with the local horizontal and pointing to the accelerator centre. Positive x is from the point of origin toward the accelerator, negative x is from the point of origin outward.
- y-axis: perpendicular to the x-axis and the mean local beam direction, pointing upward. Positive y is from the point of origin upward, negative y is from the point of origin downward.
- z-axis: parallel to the beam axis.

The azimuthal and polar angle are defined by the transformation from the Cartesian coordinate system to spherical coordinates.
In experimental particle physics, the pseudorapidity η is a commonly used spatial coordinate, which describes the angle of the particle relative to the beam axis. It is defined as:

$$\eta = \frac{1}{2} \ln \left(\frac{|\vec{p}| + p_z}{|\vec{p}| - p_z} \right) = - \ln \left[\tan \left(\frac{\Theta}{2} \right) \right], \tag{3.1}$$

where Θ is the angle between the particles momentum $\vec{p}$ and the positive z-axis and p_z is the z-component of the momentum. The reason for the usage of the pseudorapidity η rather than the angle θ is, that differences in rapidity are Lorentz invariant under boosts along the z-axis and the particle production in the collision is more or less constant as a function of pseudorapidity.

3.2. The Inner Tracking System

The ITS is the innermost detector of the ALICE apparatus and therefore the closest to the interaction point. It consists of six layers of silicon detectors, which cover the full azimuth and are arranged at radii in the range $r = 3.9 - 43.6\,\text{cm}$. Three different technologies for particle detection and signal generation are used within this detector. The first two layers are Silicon Pixel Detectors (SPD), the third and fourth layer consist of Silicon Drift Detectors (SDD) and the last two layers are Silicon Strip Detectors (SSD). All layers are mainly used for tracking, the SPDs contribute importantly to vertex reconstruction, which results in a resolution of the reconstructed vertices better than $100\,\mu\text{m}$. The SDD and SSD provide additionally specific ionization energy-loss information, which can be used for Particle Identification (PID), especially for particles with low momenta [4].

3.3. The Time Projection Chamber

The TPC is the main tracking detector of the central barrel and provides, together with the other central barrel detectors, charged-particle momentum measurements with good two-track separation, particle identification and vertex determination [12]. The TPC has full azimuthal acceptance and covers a pseudorapidity range of $|\eta| \leq 0.9$. It has a drift volume of $90\,\text{m}^3$ filled with a mixture of Neon or Argon and CO_2 and is positioned at a radius from 85 to $247\,\text{cm}$. It is divided into 18 azimuthal sectors, which are split into halves by the central electrode, as depicted in Figure 3.2. Primary electrons, which are produced by ionization of the gas in the chamber by charged particles passing the detector, are transported over a distance of up to $2.5\,\text{m}$ in the electric field from either side of the central electrode to the endplates, where the electrons are accelerated and an avalanche effect in the vicinity of the anode produces further ions which generate a signal in a system of multi-wire proportional chambers with cathode pad read-out. The readout chambers are organized in rows of pads, the inner ones (IROC) are smaller ($4 \times 7.5\,\text{mm}^2$) than the outer ones (OROC) ($6 \times 15\,\text{mm}^2$) because of the radial dependence of the track density [10]. With this setup, the x- and y-positions of the tracks can be easily determined, while the drift time is used to calculate the z-position. Hence, the readout chambers provide up to 159 three-dimensional space points and additional energy-loss information per charged particle, which can be used for tracking and PID.

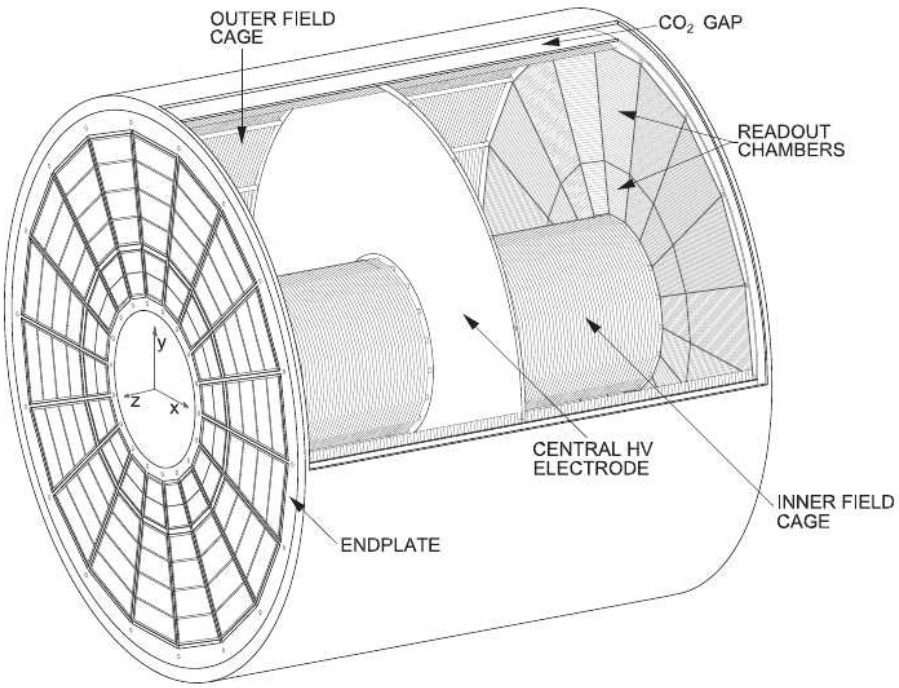

Figure 3.2.: schematic representation of the ALICE time projection chamber [13]

3.4. The Time Of Flight detector

Another detector to identify charged particles in the intermediate momentum range in ALICE is the TOF detector. It has a cylindrical shape like the other central-barrel detectors and covers, besides the full azimuth, a pseudorapidity range of $|\eta| \leq 0.9$. The detector has a modular design with 18 sectors, each of these divided into 5 modules along the beam direction and equipped with a total of 1638 Multi-gap Resistive Plate Chambers with an intrinsic resolution of ~ 40 ps [14]. The overall resolution, also considering the calibration, the momentum resolution and resolution on the start time of an event is $\sim$80 ps. In order to distinguish particles, the flight-time from the collision to the large radius of $\sim$3.7 m of the TOF is used in combination with the determined momentum and track length of the particle obtained from the tracking detectors to calculate the particle β and thus its mass. The exact procedure is outlined in subsection 3.6.2.

3.5. Event reconstruction

The event reconstruction in the central-barrel is carried out in several steps, which will be outlined briefly here. A more accurate description can be found at [4]. At first, the detector data is converted to so-called clusters, which are characterized by position, signal amplitudes, signal times and other measured quantities together with their associated errors. After that, a preliminary interaction

vertex is determined using clusters in the two SPD layers. For that, the space point is found, in which the maximum number of tracklets (lines defined by pairs of clusters) converge. This vertex is assumed to be the primary interaction point. After the preliminary vertex determination, the actual track reconstruction can be carried out following the *inward-outward-inward* scheme.

1. **Inward propagation**
   The track reconstruction starts at a large radius in the TPC because the track density is low in this region and it is therefore easier to identify tracks. Seeds are built with several TPC clusters and the vertex point. These seeds are propagated inwards, and at each step, they are updated with the nearest cluster within a proximity cut. Only tracks with at least 20 clusters and that do not miss more than 50% of the expected clusters at the end of the propagation at the inner TPC radius are accepted. The reconstructed TPC tracks are propagated to the outermost ITS layer, which is then used as a seed for track finding in the ITS. Similarly to the TPC track finding, the seeds are propagated inwards, updated at every step with a cluster that fulfills a proximity cut. In order to account for the detection inefficiency, seeds without an update at a given layer are also used for further track finding, but the χ^2 of these tracks is increased by a penalty factor for a missing cluster.
2. **Outward propagation**
   After the ITS reconstruction, all tracks are extrapolated to the point of closest approach to the preliminary interaction vertex, and the outward propagation starts. The tracks are refitted using the Kalman filter [15] and at each step, the track length integral and the time of flight are updated. When the track reaches the TRD, an attempt is made to match it with TRD clusters. The same is done in the TOF detector, and the algorithm tries to do further propagation to outlying detectors like EMCal, PHOS and HMPID.
3. **Final refit (inwards)**
   At the final stage of the track reconstruction, all tracks are propagated inwards again, starting at the outer radius of the TPC. In this process, outlier clusters are removed from the track candidates. The tracks are refitted and position, direction, inverse curvature, and associated covariance matrix are determined.

The last step is the final determination of the interaction vertex. For this, global tracks (ITS+TPC) are taken into account to find the interaction vertex with higher precision than by only using the SPD layers.

3.6. Particle identification

As stated in section 3.2, section 3.3 and section 3.4, the central-barrel detectors provide information that can be used for charged particle identification. Since this will be utilized to extract deuterons later, it will be elaborated here in more detail for the ITS, TPC and TOF detectors. For all methods of particle identification, the momentum and charge of the particles are needed. These characteristics can be obtained by considering the curvature of the particle track since the particles move in a magnetic field and the Lorentz force acts on them. For example, the momentum p for a non-relativistic particle with mass m, charge q and the bending radius r in a uniform magnetic field B can be described by

$$p = qBr \tag{3.2}$$

3.6.1. ITS and TPC particle identification

The ITS and TPC particle identification is based on the specific energy-loss of the particles in a medium, which represents, combined with the charge and momentum of the particles, a characteristic quantity for each particle species. The average specific energy loss is described theoretically with the Bethe-Bloch formula and can be parametrized as follows [4]:

$$f(\beta\gamma) = \frac{P_1}{\beta^{P_4}} \left(P_2 - \beta^{P_4} - \ln\left(P_3 + \frac{1}{(\beta\gamma)^{P_5}} \right) \right) \tag{3.3}$$

where β is the particle velocity, γ is the Lorentz factor, and P_{1-5} are fit parameters. In the ITS, the SSD and SDD layers provide specific ionization energy-loss signals, the d*E*/d*x* in each layer can be calculated by taking into account the cluster charge and the track path length in the sensor. In order to get an overall ITS d*E*/d*x* for a track, a truncated mean is calculated. In the case of four measured clusters, the average of the lowest two clusters is used, if only three clusters are available, a weighted sum of the lowest (weight 1) and the second-lowest point (weight 1/2) is utilized. An example distribution of the energy-loss signal in the ITS, based on the data later used in the analysis, is shown in Figure 3.3. One can clearly see a good separation power, especially for low momenta, where the ITS is commonly used for particle identification. In contrast to this, the TPC provides particle identification over a large momentum range and with a good resolution for tracks with many clusters. Each of the at maximum 159 clusters may provide information about the specific energy-loss. Figure 3.4 shows the d*E*/d*x* vs. *p/z* distribution for the data used in this analysis together with the corresponding splines. Splines in this context are parametrizations of the Bethe-Bloch formula, that are fitted to the specific energy-loss signals of the particles.

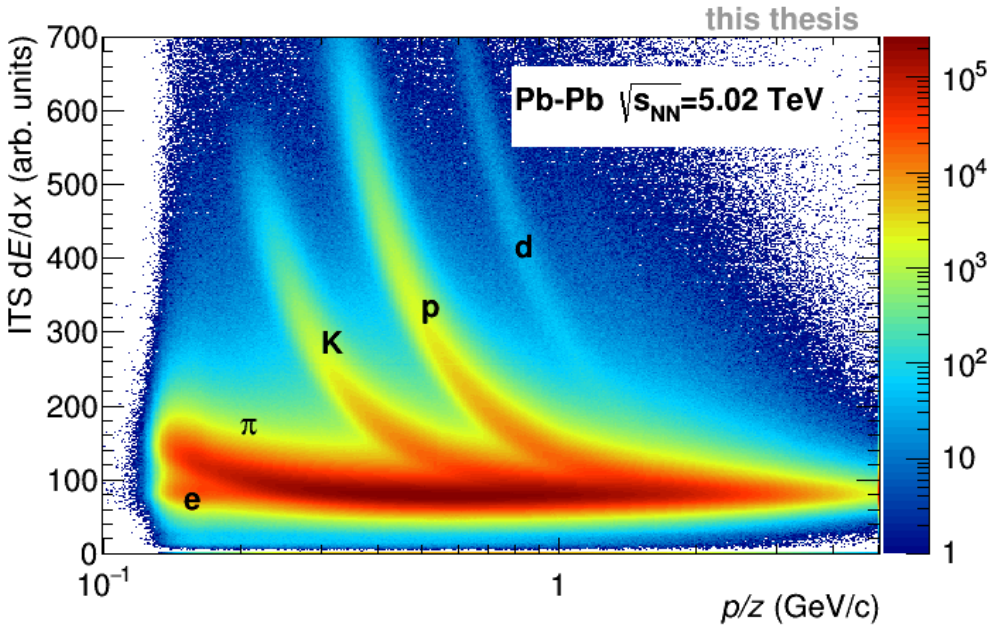

Figure 3.3.: Distribution of the specific energy-loss signal in the ITS as a function of the rigidity p/z. Produced with data, that was also used for the later analysis.

In the case of nuclei like deuterons, the splines are usually computed from the proton parametrization instead of fitting the specific energy-loss distribution of these particles. This is done by calculating the $\beta\gamma$ to the corresponding particle momentum p for the particle with mass m using Equation 3.4.

$$\beta\gamma = \frac{p}{cm} \tag{3.4}$$

These splines are also the key to the selection of particles via the specific energy-loss. The most commonly used discriminating variable for PID is the n_σ variable defined as the deviation of the measured signal (S_i) from the expected one ($\bar{S}_i$) (according to the Bethe Bloch parametrization in the case of ITS and TPC) for a species i in terms of the detector resolution σ_i:

$$n_\sigma = \frac{S_i - \bar{S}_i}{\sigma_i} \tag{3.5}$$

This variable can be used to select particles of a given species. For example a 3σ selection of deuterons in the TPC means, that all particles are selected, whose signal differs not more than three times the resolution of the detector from the expected signal according to the spline parametrization. An example for this is given in Figure 3.4, where the spline for deuterons is depicted as well as the 3σ range.

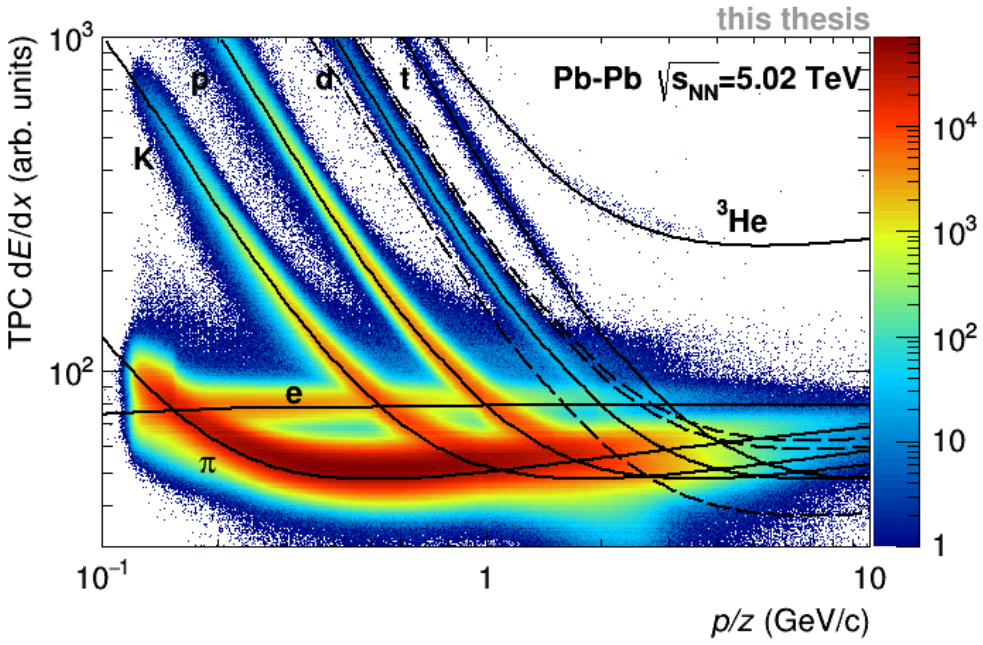

Figure 3.4.: Specific energy-loss in the TPC as a function of rigidity. The lines show the parametrization of the energy loss according to splines. Dashed lines represent the 3σ ranges. Produced with data, that was used for the later analysis.

3.6.2. TOF particle identification

The TOF detector is also able to identify particles in the intermediate momentum range by the use of the relationship between the particle mass m, velocity β and momentum p:

$$p = \gamma c m \beta \tag{3.6}$$

The velocity β can be calculated with the track length L and the time of flight t_{TOF}:

$$\beta \mathrm{c} = \frac{L}{t_{\mathrm{TOF}}} \tag{3.7}$$

Similarly to the ITS and TPC, a n_σ can be defined for the TOF, but in this case with the expected β for a specific momentum and particle species. Figure 3.5 depicts the dependency of β and p. A large continuous background contribution is visible, which originates from wrongly assigned TOF clusters to the tracks. The clusters are mainly wrongly assigned because of two effects. Firstly, since the TRD, which consists of a relatively large amount of material, lays in between the TPC and the TOF detector, the distance between these detectors is large, and scattering and energy-loss happens, which leads to larger associated uncertainties in the reconstruction to the TOF. Secondly, random hits occur in the TOF, for example by particles coming from the outside of the detector.

These could be assigned wrongly to tracks if they are in the vicinity of the expected TOF hit. This effect is also responsible for particles that seem to have a β larger than 1. The number of mismatches is larger for high multiplicity Pb-Pb collisions because mismatches increase with the track density.

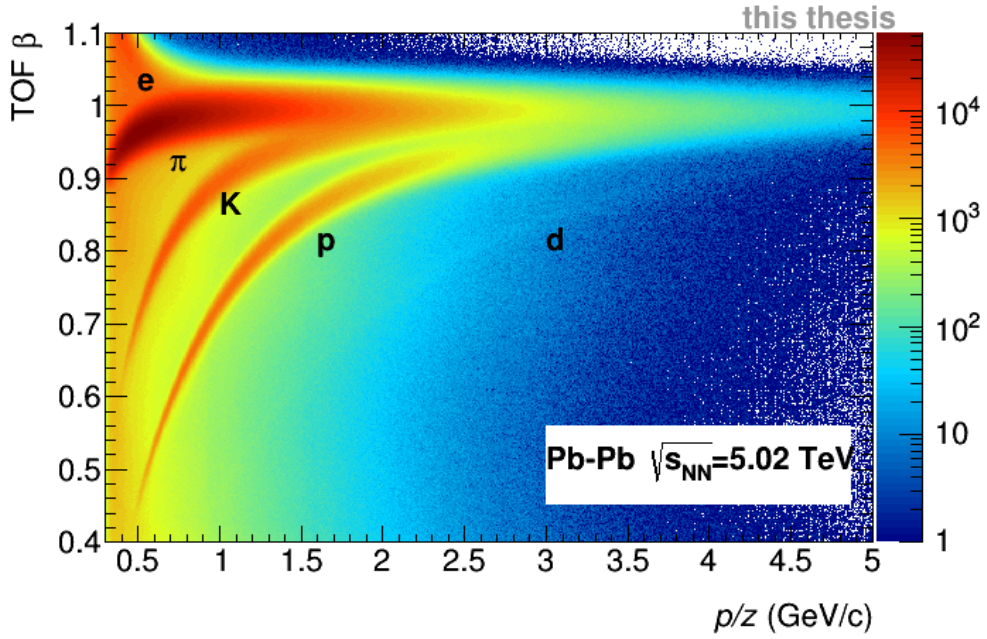

Figure 3.5.: Distribution of the particle velocity β, calculated with TOF t_{TOF}, as a function of the rigidity for particles reaching the TOF. Produced with data used for this analysis.

3.7. Monte Carlo simulations

The recorded data in ALICE is mostly accompanied by simulated events, which are also known as Monte Carlo (MC) productions. In these productions, collisions are simulated with different MC generators like PYTHIA, DPMJET, or HIJING and the detector responses are simulated by an algorithm called GEANT [16]. Monte Carlo events are especially useful when efficiencies and acceptance corrections are calculated or the differences between the true and reconstructed observables are studied. In MC, there is more information available, which represents the "true" behavior of the particles in the detectors. These information can be used to cross check the performance of reconstruction and PID in the analysis.

4. Deuteron selection and discrimination criteria

The analysis carried out in this thesis is divided into three parts as already stated in the beginning. The first part, namely the selection of primary and secondary deuterons as well as possible new discrimination criteria for primary deuterons and their secondary component, will be outlined in the following.

4.1. Data

The data used for the first part of this analysis was taken at the end of 2015 in Pb-Pb collisions at a center of mass energy of $\sqrt{s_{\mathrm{NN}}} = 5.02\,\mathrm{TeV}$ with ALICE. The utilized eleven runs are characterized by a low interaction rate and the total number of considered events sums up to 3.3 million. An event selection was carried out in order to reduce possible biases and to ensure a uniform detector response for all events. One possible bias are events that correspond to more than one collision (pile-up) or where interactions with gas in the beam pipe occur. These contributions can be removed by for example considering the number of primary vertices reconstructed with the SPD. In order to obtain a symmetrical acceptance of the detectors, commonly a geometrical selection of the events is made, here, events are selected whose primary vertex is within a range of 10 cm around the nominal collision point in the beam direction. Furthermore, in order to ensure a good quality of the particles attributes like momentum, position or specific energy-loss, a track selection is performed. The track selection criteria are given in Table 4.1. The first selection criterion of the pseudo-rapidity range $|\eta|$ ensures, that the detectors used for the analysis cover the angle in which the particles traverse the detectors. The requirement of at least 70 clusters in the TPC and 2 clusters in the ITS guarantee a good tracking quality. Furthermore, the condition of $\chi^2_{\mathrm{TPC}}/n_{\mathrm{TPCclusters}} \leq 4$ removes tracks that were not reconstructed properly in the TPC. Moreover, particles are rejected, whose trajectory has a kink for example because of a decay process. In addition to these track selection criteria, a very loose selection was done with respect to the DCA in order to get as many secondary particles as possible. This was also the reason why no requirement for the SPD was set since without a requirement tracks from secondary particles that originate from outer layers of the ITS are considered, too. The last selection criterion that was used limits the squared sum of the DCA_{xy} and the DCA_z to be below the squared sum of the maximum allowed values for the DCA_{xy} and the DCA_z.

Table 4.1.: Track selection criteria

variable	selection criterion
$\mid \eta \mid$	≤ 0.8
$n_{\mathrm{TPCclusters}}$	≥ 70
$n_{\mathrm{ITSclusters}}$	≥ 2
$\chi^2_{\mathrm{TPC}}/n_{\mathrm{TPCclusters}}$	≤ 4
accept kink daughters	kFALSE
$\mid \mathrm{DCA}_{xy} \mid$	≤ 2.4 cm
$\mid \mathrm{DCA}_{z} \mid$	≤ 3.2 cm
SetDCAToVertex2D	kTRUE

4.2. Deuteron selection

Because this thesis focuses on primary and secondary deuterons, these particles need to be extracted from the data which consists of various particles (e, π, K, p, d, t, ^{3}He, etc.) that are produced in the collisions. This particle selection is done by using the PID information provided by the ITS, the TPC and the TOF detector as stated in section 3.6. Up to a momentum of 0.9 GeV/c, the TPC and ITS are used to identify and select deuterons. In this region, the TPC provides a relatively clear selection via the energy-loss, the additional ITS selection was made due to some contamination in the ITS signal after selecting only by TPC. The selection of the particles was made by considering the n_σ variable, that was already introduced in section 3.6.

Table 4.2.: deuteron selection criteria

detector	selection	momentum range
ITS	-3σ to 4σ	full range
TPC	$\pm 3\sigma$	full range
TOF	$\pm 3\sigma$	above 0.9 GeV/c

For the TPC, a 3σ-selection was performed, whereas for the ITS an asymmetric selection of -3σ to 4σ was applied because the spline, that was used for the deuteron description, was off-centered. This effect occurs, since the splines for deuterons are calculated from the proton spline instead of fitting the Bethe Bloch parametrization to the distribution, as explained in subsection 3.6.1 and therefore additional effects for deuterons, that may occur and influence the signal are not considered. In the momentum range above 0.9 GeV/c, additionally to the TPC and ITS, the TOF detector contributed to particle selection. With this detector, particles were selected within a 3σ-range of the expected signal. This was done because selection in the intermediate momentum range is becoming increasingly difficult due to similar energy-loss signals in the ITS and TPC, while the TOF provides a rather good selection, but lowers the efficiency significantly. In the higher p_{T}-

range the selection becomes even more difficult and some contamination can be expected by other particles. However, this circumstance has only a minor influence on the following analysis, since secondary particles produced in the detector material barely exceed a momentum of 2 GeV/c. The signal of the selected deuterons are given in Figure 4.1, Figure 4.2 and Figure 4.3 in comparison to the signals of all measured particles. Furthermore, the selection criteria are summarized in Table 4.2.

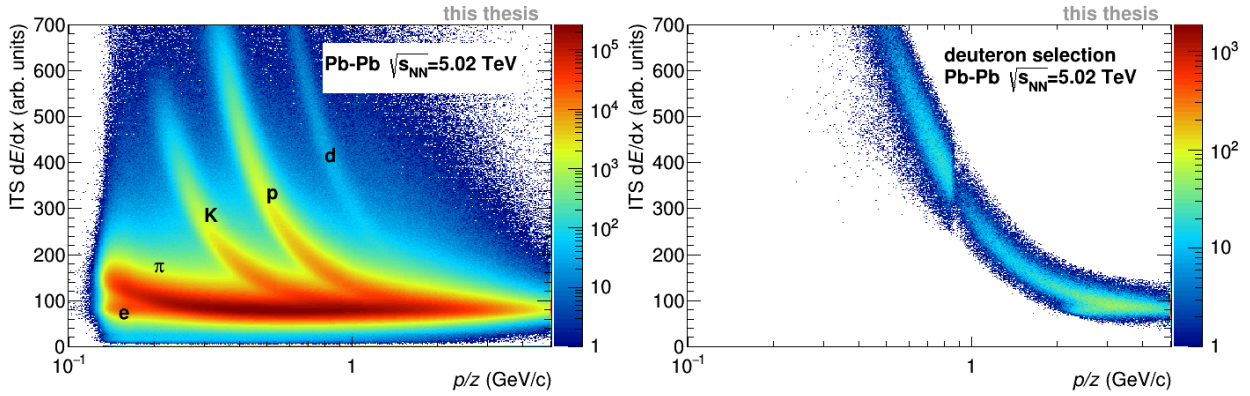

(a) without selection (b) selected deuterons in ITS

Figure 4.1.: Specific energy-loss signal in the ITS as a function of p/z for all particles (a) and for selected deuterons (b). An asymmetric selection was performed due to a off-centered spline. The edge at 0.9 GeV/c is due to the additional TOF selection, which lowers the efficiency.

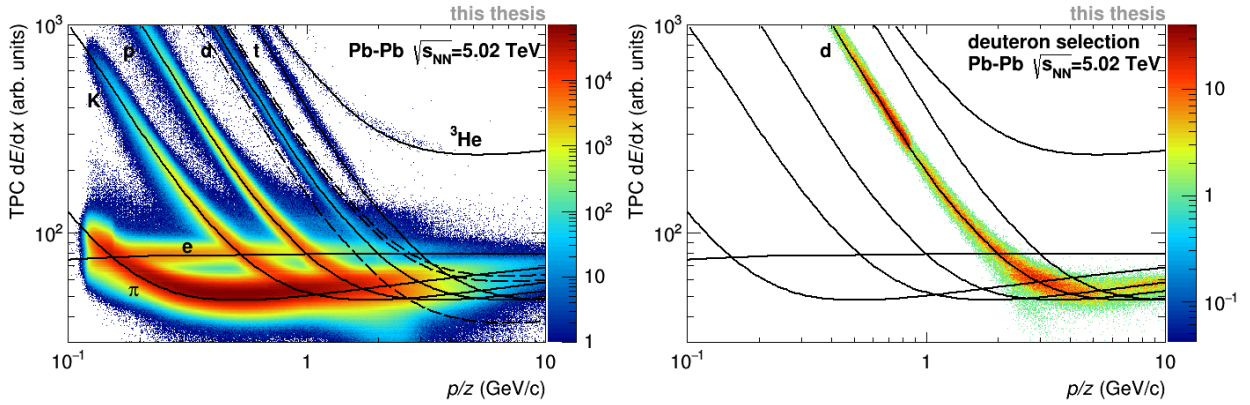

(a) without selection (b) selected deuterons in TPC

Figure 4.2.: Specific energy-loss signal in the TPC as a function of p/z for all particles (a) and for selected deuterons (b). In higher momentum range there may be some contamination. Selection made as mentioned above.

To validate the quality of the deuteron selection, the distribution of the n_σ variable for different rigidities p/z is taken into account. In principle, the n_σ distribution for a given momentum follows a Gaussian distribution with a width of one and a mean of zero in the first order, since the particles scatter statistically around the expected value. An example for the Gaussian behavior is given

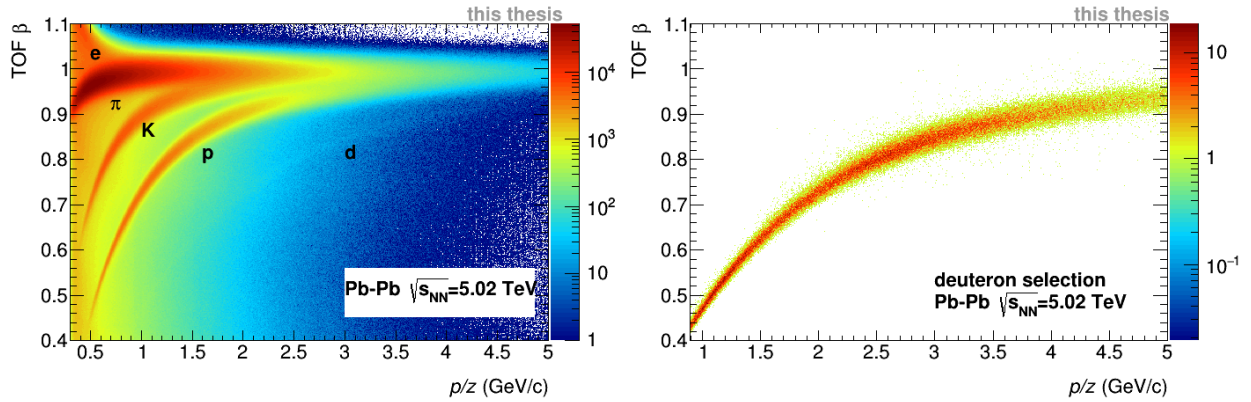

(a) without selection (b) selected deuterons in TOF

Figure 4.3.: TOF β signal as a function of p/z for all particles (a) and for selected deuterons (b). The background in (a) is mainly due to TOF mismatches as stated in subsection 3.6.2

in Figure 4.4 (left), where the n_σ distribution of the TPC is depicted in a momentum range of 0.7-0.8 GeV/c.

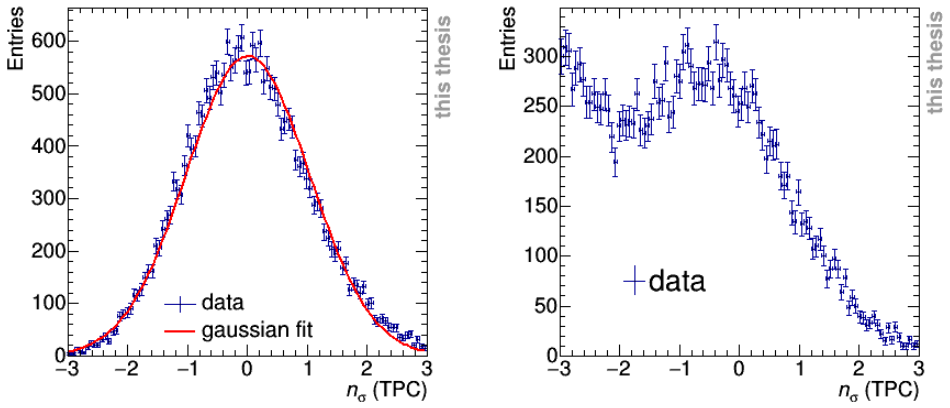

Figure 4.4.: nσ-distribution for the TPC in momentum ranges from 0.7-0.8 GeV/c and 2.3-2.5 GeV/c.

However, the n_σ distributions for the different detectors are not over the full momentum range shaped like a Gaussian with the width of 1, as it is visible in Figure 4.5, where the n_σ distributions are depicted. This is mainly the result of two different effects. The first effect are the already above mentioned calculated parametrizations of the signals (see subsection 3.6.1), which lead to off-centered distributions since additional effects for deuterons are not considered. For the TPC and TOF this effect is rather small, whereas for the ITS this leads to significant deviations from the expected distribution and a shift of the mean of the distribution. The second effect is the contamination by other particle species. This effect occurs mainly for higher momenta, for example in the region between 2 and 3 GeV/c, since the separation power of the detectors decreases in this momentum range. The contamination is clearly visible in Figure 4.4 (right) and in Figure 4.5, Fig-

ure 4.1 and Figure 4.2. Also for high momenta above 6 GeV/c, the contribution by other particles is visible in Figure 4.5. Furthermore, a strong shift in the momentum range from 1 to 2 GeV/c for the TOF detector can be noticed. The origin of this shift could not be fully clarified, but since the selection of deuterons in the TPC and ITS is accurate in the region where the shift occurs, contribution by other particles is unlikely. Therefore no further investigations were carried out. The effect of off-centered parametrizations could have been eliminated by re-centering of the distributions, but this was not done, since the selected deuteron sample is sufficiently pure and large enough for further investigations, especially in the momentum region, where secondary deuterons occur (up to 2 GeV/c).

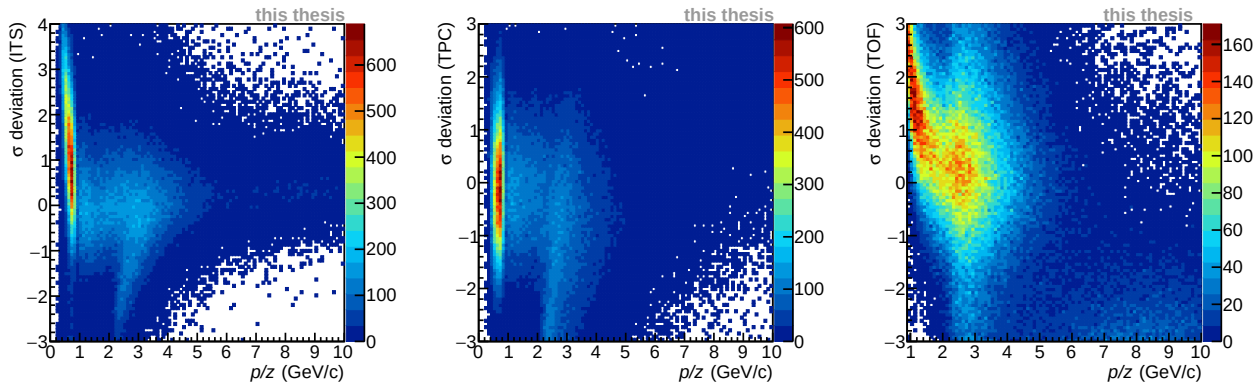

Figure 4.5.: nσ-distributions for ITS, TPC and TOF.

4.3. Separation of primary and secondary deuterons

In order to study the distributions of variables, that might be useful for discrimination of primary and secondary deuterons, at first, samples of primary and secondary deuterons have to be created. The sample for primary deuterons can be filled with anti-deuterons since they are not produced via the spallation process (see chapter 1) and the decay of the anti-hyper-triton contributes only with a negligibly small fraction to all anti-deuterons. To obtain a sample for secondary deuterons produced by spallation a more sophisticated approach has to be applied. This is done via a DCA selection of the deuteron sample, which will be discussed in the following.

4.4. Secondary deuteron selection

In order to create a sample of secondary deuterons, the primary deuterons need to be separated from the secondary ones. The separation is done by excluding the DCA region around zero, where primary particles occur. For this, the maximum width of the DCA distribution of primary deuterons was approximately estimated. The DCA selection for the secondaries (only for deuterons) was then performed as follows:

$$(|\mathrm{DCA}_{xy}| \geq 0.12\,\mathrm{cm}) \text{ or } (|\mathrm{DCA}_{z}| \geq 0.12\,\mathrm{cm})$$

The accuracy of this selection was verified in chapter 5, where the resolution was studied in more detail. The selected range excludes at least 4σ of the primaries in xy and 3σ in z in every momentum range. The selection could have been made narrower for the DCA_{xy}, retrospectively, but since the number of secondary deuterons was large enough for the further investigations, the selection is sufficiently good. In addition to this, only particles with a momentum up to 3 GeV/c were selected. This was done, since deuterons that are produced via the spallation process, do not exceed this value. For consistency, this momentum selection criterion was also applied to the sample of primary deuterons.

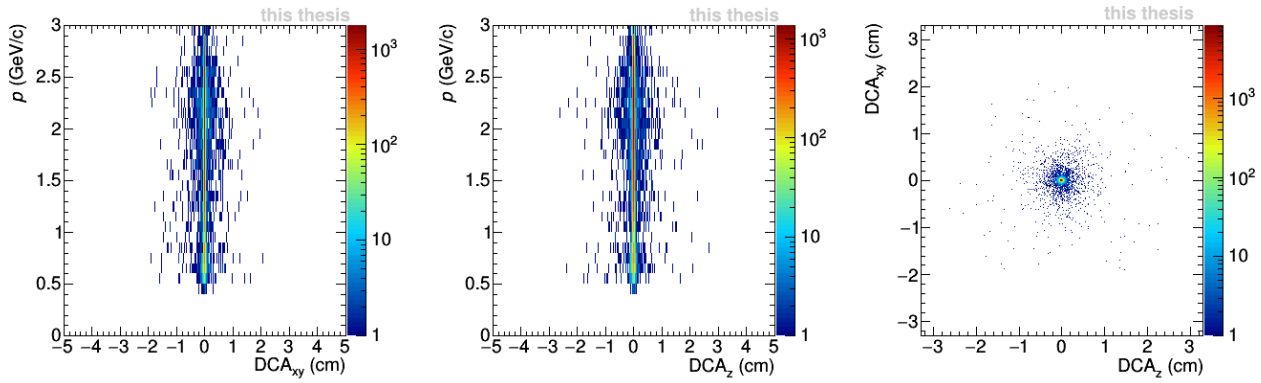

Figure 4.6.: Momentum p vs. DCA_{xy} and DCA_{z} for primary anti-deuterons (left and middle). Correlation between DCA_{xy} and DCA_{z} (right).

In Figure 4.6 and Figure 4.7 the momentum vs. DCA distributions of the selected samples for primary anti-deuterons and secondary deuterons are shown as well as the correlation between the DCA_{xy} and DCA_{z}. The DCA distributions for the anti-deuterons are narrow as expected because these particles only form in the initial collision and therefore their distance to the primary vertex is zero within the resolution of the interaction point and the track. The selected secondaries have in comparison a much wider DCA distribution. The DCA_{xy} and DCA_{z} are not correlated for secondary deuterons in contrast to the primary deuterons, which means they can be investigated separately. The elliptical form of the DCA distribution (Figure 4.7 (right)) is due to the track selection criteria.

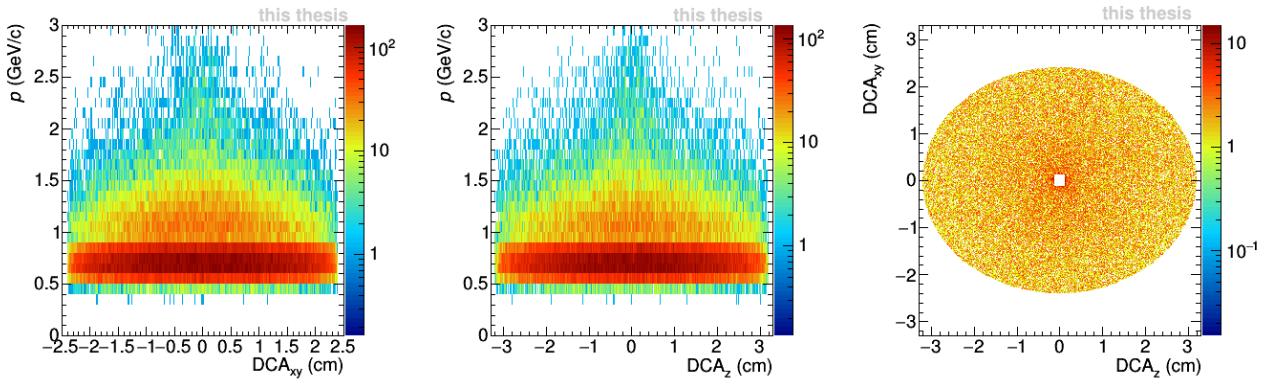

Figure 4.7.: Momentum p vs. DCA$_{xy}$ and DCA$_z$ for secondary deuterons, selected with the criteria mentioned above (left and middle). Correlation between DCA$_{xy}$ and DCA$_z$ (right). Elliptical form of distribution is due to track selection criteria.

4.5. Possible new criteria for primary deuteron selection

This section is dedicated to one of the main goals of this thesis: Finding possible new selection criteria and improving old ones to achieve good discrimination between primary and secondary deuterons. For this, the distributions of different variables are studied for the primary and secondary deuteron samples.

4.5.1. ITS hits

Secondary deuterons are produced by the spallation process in the material of the detectors, for example in the ITS, whereas primary deuterons always originate from the primary interaction vertex. Therefore, it can be expected, that secondary deuterons are more unlikely to have a hit in one of the first two ITS layers. To verify and quantify this, the percentage of tracks with hits in a specific ITS layer i was determined as well as the total number of hits in the ITS for the two deuteron samples of primary and secondary deuterons. The histograms are shown in Figure 4.8.

In Figure 4.8 (a) it is evident, that most secondary deuterons lack of hits in the first two ITS layer. Only $\sim$38% of the selected secondary deuterons have a hit in the first SPD layer and $\sim$68% in the second one. In comparison, about 78% of primary deuterons have a hit in the first layer and 90% of one in the second layer. In the outer layers, the percentage of hits remains constant for primary deuterons, whereas it increases for secondary deuterons until the fifth layer is reached. This can be explained by the fact, that a certain amount of secondary deuterons is produced by the spallation process in each ITS layer. Therefore, the total amount of secondary deuterons increases after each layer. The converging effect in the last two layers for secondaries is due to the ITS requirement of at least two ITS hits. In order to eliminate most of the secondary deuterons, a requirement of a

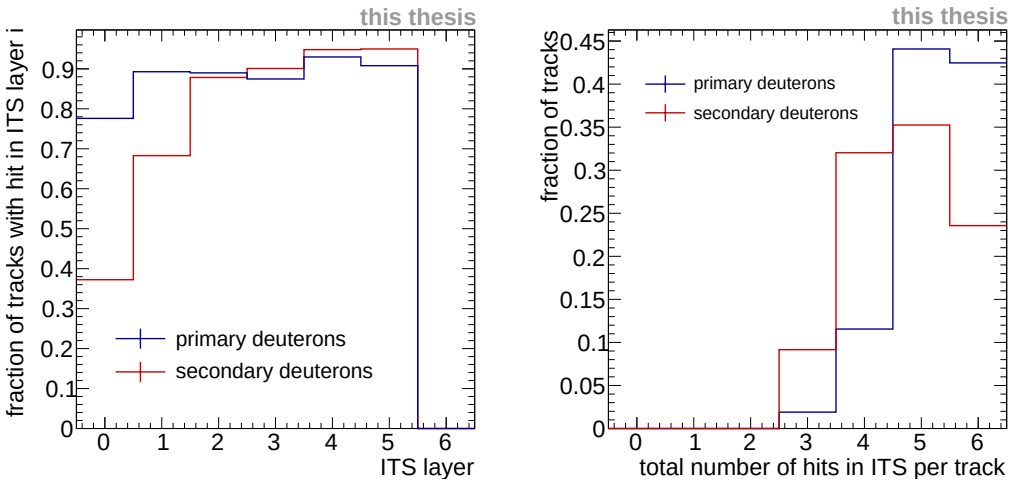

(a) hits in ITS layer

(b) total number of hits

Figure 4.8.: Distribution of hits in the ITS for primary and secondary deuterons. A lack of hits in the first two ITS layer for secondary deuterons is visible.

hit in the first SPD layer (kFirst) or a requirement of a hit in at least one of the SPD layers (kAny) could be applied. As kAny is used in most of the analyses, the difference between kAny and kFirst is of special interest in this case. By switching from kAny to kFirst, the number of secondary deuterons can be reduced by approximately 44% while losing about 13% of primary deuterons. Figure 4.8 (b) shows in addition to (a) the total amount of hits in the ITS. This plot is directly connected to the first one, as the secondary deuterons have a lower percentage of tracks with five or six ITS hits due to their lack of hits in the first two layers in comparison to primary deuterons. In this context, a selection of tracks with at least five hits in the ITS could extract 86% of primary deuterons while excluding 41% of the secondary deuterons for the used samples.

4.5.2. Shared clusters in the ITS

In this subsection, the distribution of shared clusters will be studied. Shared clusters are clusters (in this case in the ITS), that were assigned to more than one track in the process of reconstruction. Shared clusters are of interest since their distribution is expected to be different for primary and secondary deuterons. In the process of spallation, secondary particles are produced at the point, where an incoming particle interacts with the detector. Therefore the produced particles may be assigned with the same cluster, a shared cluster. The distributions of tracks with shared clusters are illustrated in Figure 4.9. For primary deuterons, a decreasing fraction of tracks with shared clusters is noticeable for increasing ITS layers. This can be understood by the decreasing track density, which leads to a better reconstruction of the tracks and fewer shared clusters. Whilst the

distribution of shared clusters for the secondary deuterons is nearly identical to the one for primary deuterons in the last four layers, it is significantly different in the two SPD layers. In the first SPD layer 20% (8.5%) of secondary (primary) deuterons share a cluster, in the second one 11.5% (7%). This might be useful for further discrimination of primary and secondary deuterons. A requirement of no shared cluster in the first (second) SPD layer for the tracks would eliminate 20% (11.5%) of secondary deuterons, that have a hit in the first SPD layer, but it would also reduce the number of primaries by 8.5% (7%).

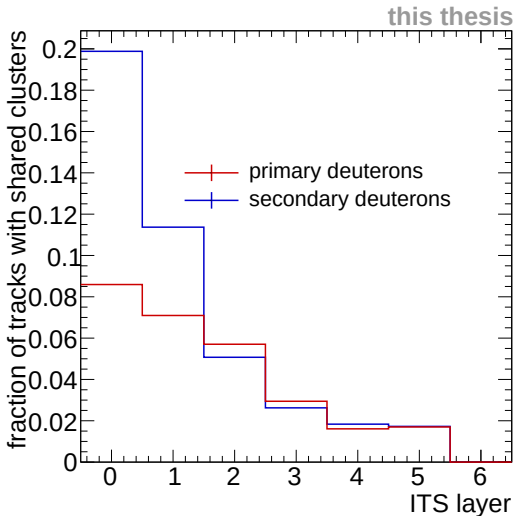

Figure 4.9.: Distribution of shared clusters in the ITS for primary and secondary deuterons. The fraction is given by the number of tracks that have a shared cluster in the specific layer divided by the number of tracks that are associated with a cluster in the specific ITS layer.

4.5.3. d*E*/d*x*-η distribution

Other useful variables for separation of primary and secondary deuterons might be the specific dE/dx energy-loss, the pseudo-rapidity η and especially their correlation. To investigate this, two histograms were filled with the dE/dx in the ITS on the y-axis and the pseudo-rapidity η on the x-axis for primary and secondary deuterons. They are depicted in Figure 4.10. Primary and secondary particles differ clearly in the energy-loss, whereas the pseudo-rapidity distributions are similar. Primary particles a characterized mostly by an energy-loss of 100-200 keV/300 μm, while secondary particles can be associated with an average energy-loss of 200-600 keV/300 μm. However, the difference in the dE/dx can be fully attributed to the different momentum distributions of primary and secondary deuterons, which are depicted in Figure 4.10 (right). Most of the secondary deuterons are within a momentum range of 0.5-1.5 GeV/c, whereas primary deuterons mostly have a momentum above 1.5 GeV/c. This is via the Bethe-Bloch formula directly connected to the energy-loss, secondary deuterons are characterized therefore by a much higher energy-loss than primary ones. In order to verify, that this is the only effect having an impact on the distributions, some further checks were carried out. Within these checks, the distributions of the dE/dx vs. η were studied for narrow momentum regions to eliminate the effects of the momentum distributions. No difference between primary and secondary deuterons was found.

The pattern in the histogram for the secondary particles is due to the TOF structure. This pattern is only visible up to an energy-loss of about 300 keV/300 μm, which is caused by the particle selection; particles with higher energy-loss are in a momentum region where the TOF was not used for PID. All in all the specific energy-loss, as well as the pseudo-rapidity, cannot be used for better discrimination of primary and secondary deuterons.

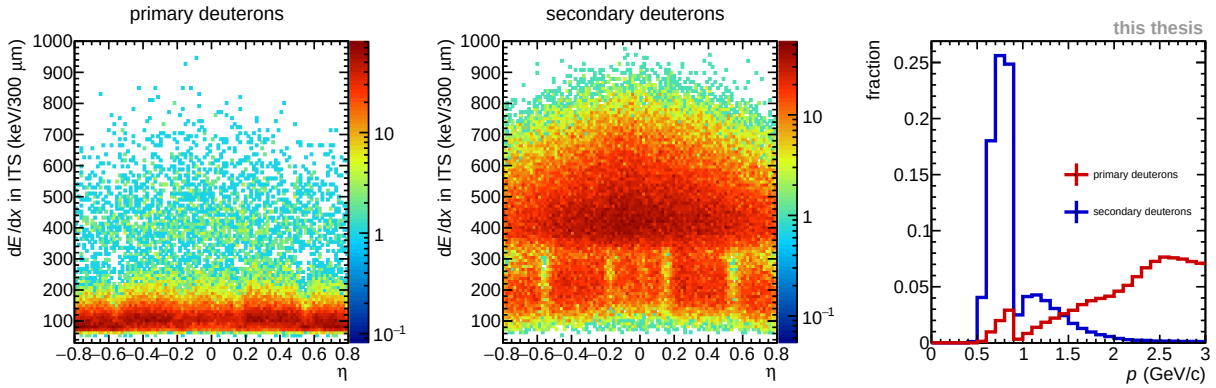

Figure 4.10.: distribution of ITS dE/dx vs. pseudo-rapidity η for primary (left) and secondary (middle) deuterons. On the right one can see the normalized momentum distributions for primary and secondary particles from 0-3 GeV/c.

4.5.4. Chi2/NDF-distributions for ITS and TPC

In Figure 4.12 and Figure 4.13, the χ^2/NDF vs. the momentum of the tracks are depicted for the ITS and the TPC for primary and secondary deuterons, respectively. The χ^2 is calculated in the reconstruction process and characterizes the quality of the track. The Number of Degrees of Freedom (NDF) for the detectors is, in this case, the numbers of clusters in the TPC and ITS, respectively. It could be expected that the secondary particles have a larger χ^2/NDF, especially in the ITS, as they lack some hits and may be propagated wrongly in the reconstruction algorithm. At first glance, the distributions for primary and secondary particles are different in Figure 4.12 and Figure 4.13. However, the different momentum distributions for primary and secondary deuterons have to be taken into account, since the χ^2/NDF is depicted as a function of the momentum. For this, the χ^2/NDF was studied within a narrow momentum region and the projected distributions were normalized to eliminate the effects of the momentum distributions. Examples for the χ^2/NDF distributions in the ITS and the TPC for primary and secondary deuterons in a narrow momentum region are given in Figure 4.11.

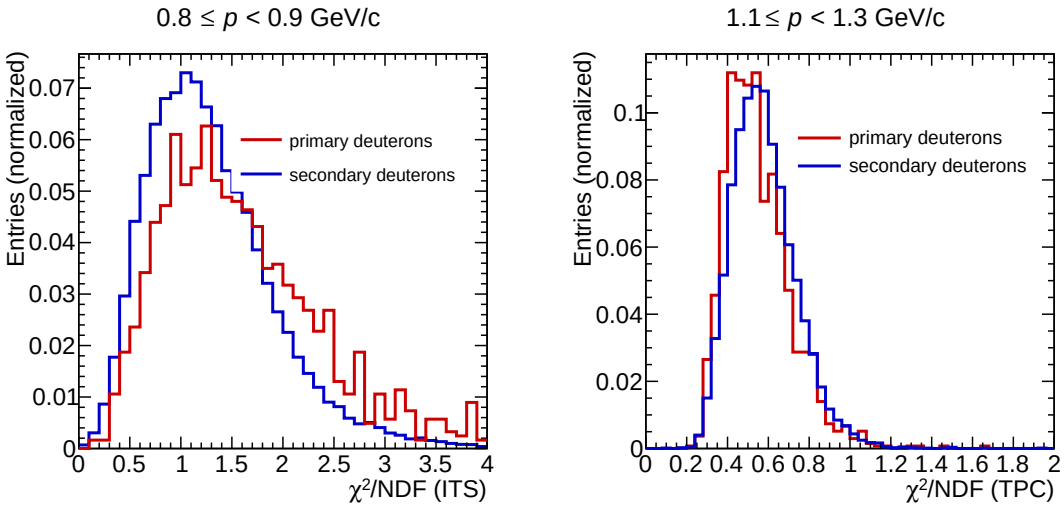

Figure 4.11.: Projections of the χ^2/NDF distribution in the ITS and TPC of primary and secondary deuterons in a specific momentum range.

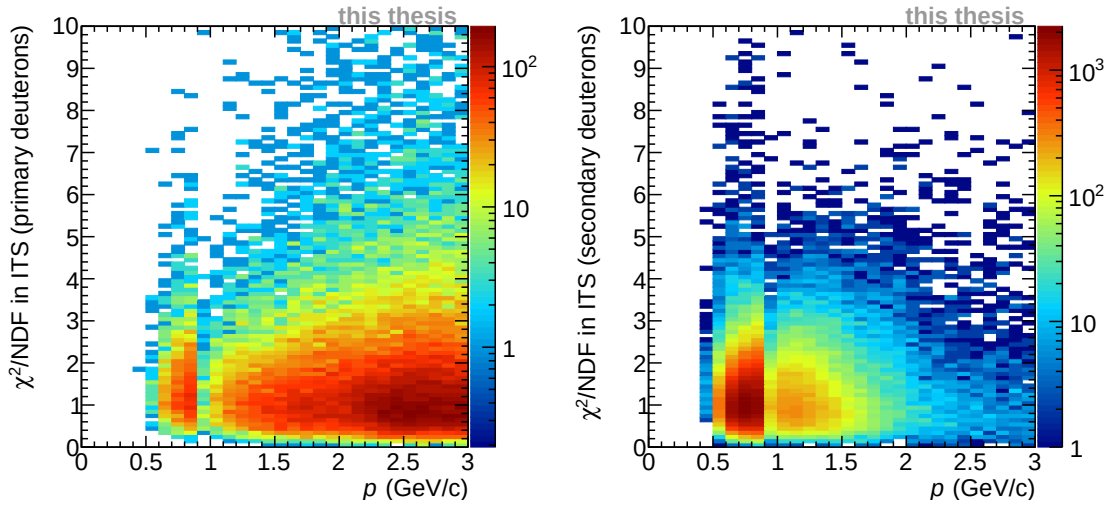

Figure 4.12.: χ^2/NDF vs. p distribution for primary (left) and secondary (right) deuterons in the ITS. The differences mainly occur due to the specific momentum distributions of the particles.

It is visible, that the χ^2/NDF distributions in the TPC are very similar, whereas for the ITS minor differences occur. The behavior in the ITS is unexpected since primary deuterons tend to higher χ^2/NDF. The reason for this could not be fully clarified. The investigations were done for all momentum ranges, but the differences between the distributions of primary and secondary deuterons were not sufficiently large to use them for discrimination of primary and secondary deuterons. Therefore the variable of the χ^2/NDF cannot be used to improve their separation. Another effect that is visible from the Figure 4.13 and Figure 4.12 is, that in comparison to the ITS, the χ^2/NDF of the TPC is in general lower, which means the tracking is better, as it was expected.

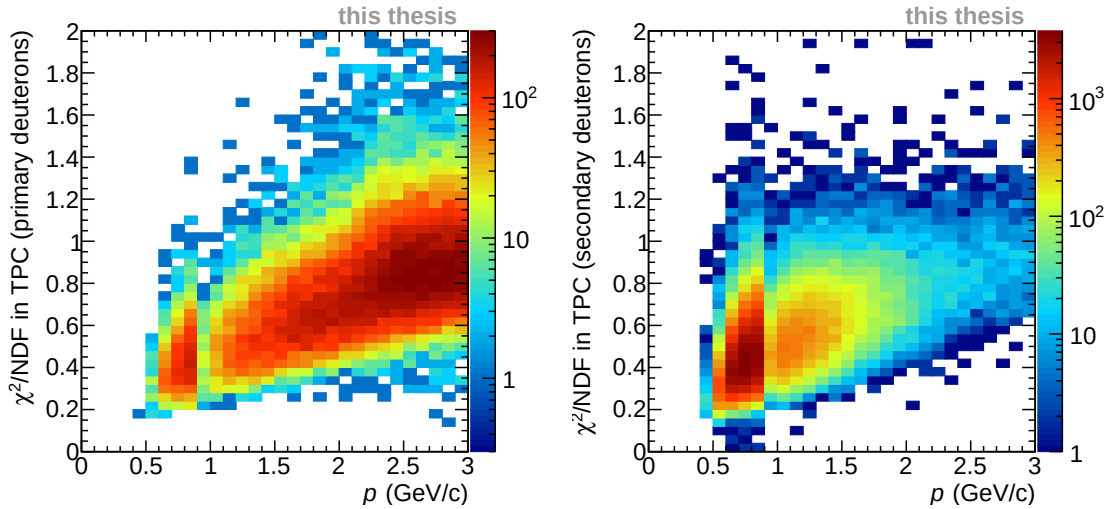

Figure 4.13.: χ^2/NDF vs. p distribution for primary (left) and secondary (right) deuterons in the TPC. The differences mainly occur due to the specific momentum distributions of the particles. Moreover, one can see a positive correlation between χ^2/NDF and p.

5. DCA resolution of anti-deuterons

This chapter is dedicated to resolution studies of anti-deuterons in order to verify the applied DCA selection in chapter 4 as well as preparing the fitting procedure used in chapter 6. For this, the behavior of the resolution will be examined for different ITS requirements and centralities.

5.1. Data

For section 5.4 and chapter 6 the number of events was increased to 60 million events and additional track selection criteria were applied. This was done to achieve better statistical precision, which is necessary for the determination of the fraction of primary deuterons carried out in the next chapter. Additional to the previous low interaction rate runs, also high interaction rate runs were taken into account. It was properly checked, that these additional runs match with the low interaction rate runs with respect to the DCA resolution (Figure A.6). The track selection criteria were adjusted to more commonly used ones since the studies of the resolution and fractions of primary deuterons will be mostly used in general analyses of deuterons. As depicted in Table 5.1, the three additional criteria are: The requirement of at least one hit in the SPD (kAny), at least 60 clusters in the TPC that were used for the calculation of the $\mathrm{d}E/\mathrm{d}x$ signal ($n_{\mathrm{TPC,dEdxclusters}}$) and at least a ratio of 60% between the crossed rows and all findable clusters for the particle in the TPC. Findable clusters are all geometrical possible clusters with respect to the track direction, whereas the number of crossed rows defines how many rows the particle crossed in the TPC. Furthermore, Monte Carlo samples are used within chapter 5 and chapter 6, which are based on the utilized data period. Two different productions were taken into account. The first sample is a general-purpose production with Hijing anchored to the measured data in Pb-Pb collisions at $\sqrt{s_{\mathrm{NN}}} = 5.02\,\mathrm{TeV}$ collected in 2015.This production was done centrality-selected for centrality ranges of 0-10%, 10-50% and 50-90%, sampling the full period with 2%, 3% and 10% of the collected data. The second MC production was obtained by injecting additional nuclei into the generated events. In this case, the following numbers of each species were injected in each event in order to obtain larger yields for investigations: 10 particles of each species up to the mass of (anti-)alpha-particles, 40 particles of hypertriton and anti-hypertriton and 20 particles of (anti-)hyper-hydrogen-4 and (anti-)hyper-helium-4, respectively. This was done in centrality ranges of 0-10%, 10-50% and 50-90%, while simulating 100k, 400k and 400k events, respectively. For the Monte Carlo samples, the exact same event and track selection criteria were applied as for the data.

Table 5.1.: Track selection criteria

variable	track selection
$\mid \eta \mid$	≤ 0.8
$n_{\text{TPCclusters}}$	≥ 70
$n_{\text{crossed rows, TPC}}/n_{\text{f.clusters, TPC}}$	≥ 0.6
$n_{\text{TPC,dEdxclusters}}$	≥ 60
$n_{\text{ITSclusters}}$	≥ 2
SPD requirement	kAny
$\chi^2_{\text{TPC}}/n_{\text{TPCclusters}}$	≤ 4
accept kink daughters	kFALSE
$\mid \text{DCA}_{xy} \mid$	≤ 2.4 cm
$\mid \text{DCA}_{z} \mid$	≤ 3.2 cm
SetDCAToVertex2D	kTRUE

5.2. Resolution

Resolution refers to the standard deviation (also known as Root Mean Square (RMS)) of the DCA distribution of primary particles, it is split into the resolution longitudinal to the beam axis ($d_{0,z}$) and in the resolution in transverse plane ($d_{0,xy}$), since the SPD is segmented differently in these directions and the resolutions differ. In principle, only a single peak at zero should be present in the distribution, since the particles all originate from the primary vertex. But the distribution is widened due to two reasons: First, the reconstructed tracks are associated with an uncertainty, which is due to limited precision of the detectors, and second, the reconstruction of the primary vertex is only possible within a certain resolution, therefore the DCA, which is the distance between the primary vertex and the track, can only be determined within a resolution limited by these uncertainties. Moreover, the resolution depends on the momentum of the particles under consideration, particles with a larger momentum can be reconstructed with higher precision, since their tracks consist of more clusters and they have a lower specific energy loss, meaning their momentum does not change much when traversing the detector setup. An example of the DCA distribution for primary anti-deuterons is given in Figure 5.1. In order to determine the resolution, the distribution was assumed to be Gaussian and therefore a Gaussian fit was performed. The standard deviation obtained from the fit was taken as the resolution of the DCA in the chosen transverse momentum range.

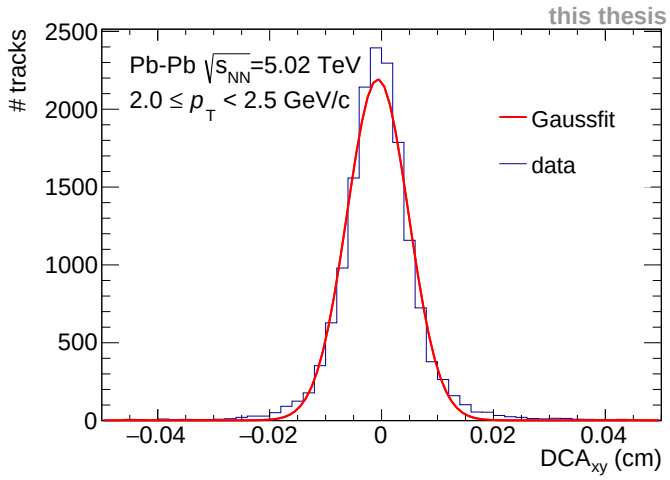

Figure 5.1.: DCA distribution for anti-deuterons in the momentum range of $2.0 \leq p \leq 2.5$ GeV/c and Gaussian fit to the distribution. A good agreement between the data and the fit is observed.

5.3. DCA resolution for different ITS requirements

At first, the resolutions of the DCA$_{xy}$ and the DCA$_z$ were determined for different requirements of the SPD in transverse momentum ranges between 0 and 10 GeV/c, as shown in Figure 5.2 and Figure 5.3.

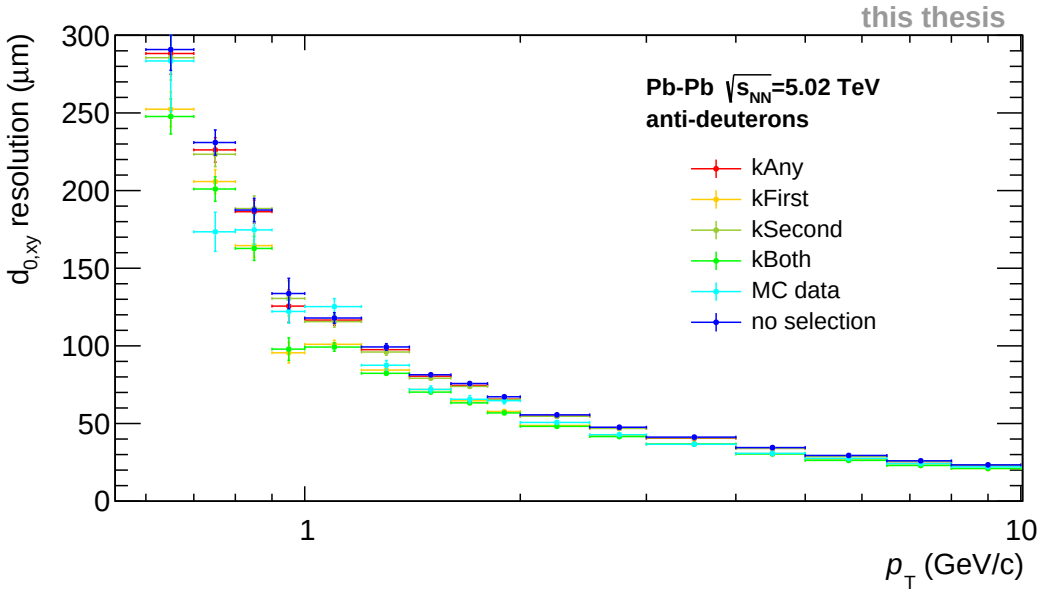

Figure 5.2.: DCA$_{xy}$ resolution vs. transverse momentum p_T for different SPD requirements for anti-deuterons. The drop at 0.9 GeV/c is due to deuteron selection.

This was done to examine the behavior of the resolution for the different requirements, which is important for the investigations of the fraction of primary deuterons. Resolutions for tracks with the following requirements were investigated: tracks with at least one hit in any SPD layer

(kAny), tracks with a hit in the first SPD layer (kFirst), tracks with a hit in the second SPD layer (kSecond), tracks with hits in both SPD layer (kBoth) and tracks with no requirements on the SPD (no selection). For comparison, the resolution determined from Monte-Carlo simulations is given as well. As expected, the tracks with the requirement kBoth have the highest resolution, because both SPD layers can be used for reconstruction, which improves the propagation to the primary vertex and minimizes the uncertainties. This is followed by tracks with the requirement of kFirst, which have a slightly worse resolution. The resolution does not differ significantly because 92% of the observed particles for kFirst also belong to kBoth. As the first SPD layer is the most important for the determination of the DCA, the requirement of kSecond, where this layer is not considered, leads to worse resolutions especially in the low momentum ranges, where the difference to kFirst and kBoth is at maximum 30 μm (8%). This effect is rather big since 20% of the tracks of kSecond do not contain a hit in the first SPD layer.

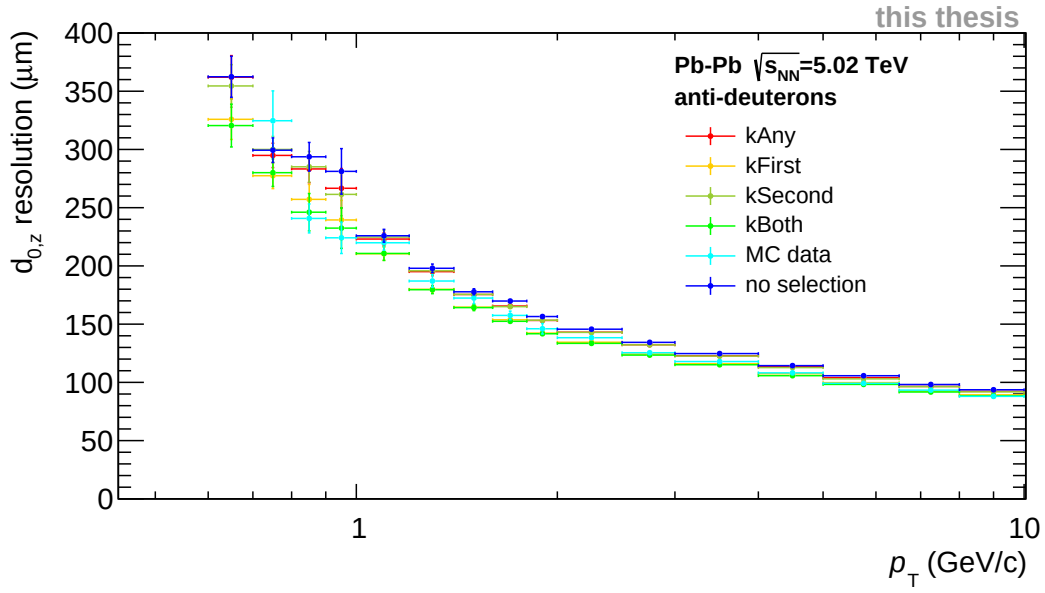

Figure 5.3.: DCA$_z$ resolution vs. transverse momentum p_{T} for different SPD requirements for anti-deuterons. Resolution is worse than in DCA$_{xy}$ as a result of the worse resolution of the detectors in the z-direction.

The resolution for the requirement of kAny is fully dominated by the resolution of the kSecond tracks, as 93% of the tracks of kAny fulfill the condition of kSecond. Similar to this is the resolution of tracks with no specific SPD requirement. This is because the fraction of tracks with no hits in both layers is small (5%) and the resolution is predominantly given by the tracks with the requirement of kAny, which contribute by 95%.

The resolution behaved in general as expected for the different requirements, as kAny, kSecond and no requirement were worse than the requirements of kFirst and kBoth, that have a hit in the first SPD layer. But these differences are not significant as most of the tracks (70%) belong to all of the groups. In addition to this, the DCA resolutions obtained from collision data and Monte-Carlo

simulations can be compared in order to verify the accuracy of the Monte-Carlo production and emphasize possible differences. Figure 5.2 depicts the behavior of the Monte Carlo simulation for primary deuterons. It is evident, that the resolutions obtained from Monte Carlo agree with the data within their uncertainties. Therefore the assumption of taking anti-deuterons as a proxy for primary deuterons is valid. Furthermore, the Monte Carlo data provides an accurate description of the resolution. This information will be used in chapter 6. When comparing the figures for the resolution of the DCA_{xy} and the DCA_{z}, it is evident, that the resolution in the z-direction is worse over all transverse momentum ranges. For example, in the momentum range from 0.6-0.7 GeV the resolution in z is about 350 μm, whereas it is below 300 μm in the xy-plane. This is a result of the detector resolutions, which are higher in the xy-plane due to the detector granularity. However, in both plots, the behavior for different SPD requirements is the same. Another present feature that is visible in Figure 5.2 and Figure 5.3 is the drop at a momentum of 0.9 GeV. This was investigated properly as this is the momentum, where the selection criteria are changed and an additional TOF selection is performed. To examine it, the resolution was also determined without the TOF selection and it was found, that this is indeed a feature of the change of selection criteria.

5.4. Centrality dependency of the resolution

Another aspect that was investigated in the course of this analysis was the centrality dependence of the resolution. This has been done because the fitting procedure introduced in the next chapter is based on the resolution studies performed in this chapter and especially the different centrality ranges are taken into account. As more central events are connected to higher multiplicities, it can be expected, that the DCA resolution is higher since the vertex reconstruction is more precise if more tracks for its reconstruction are taken into account.

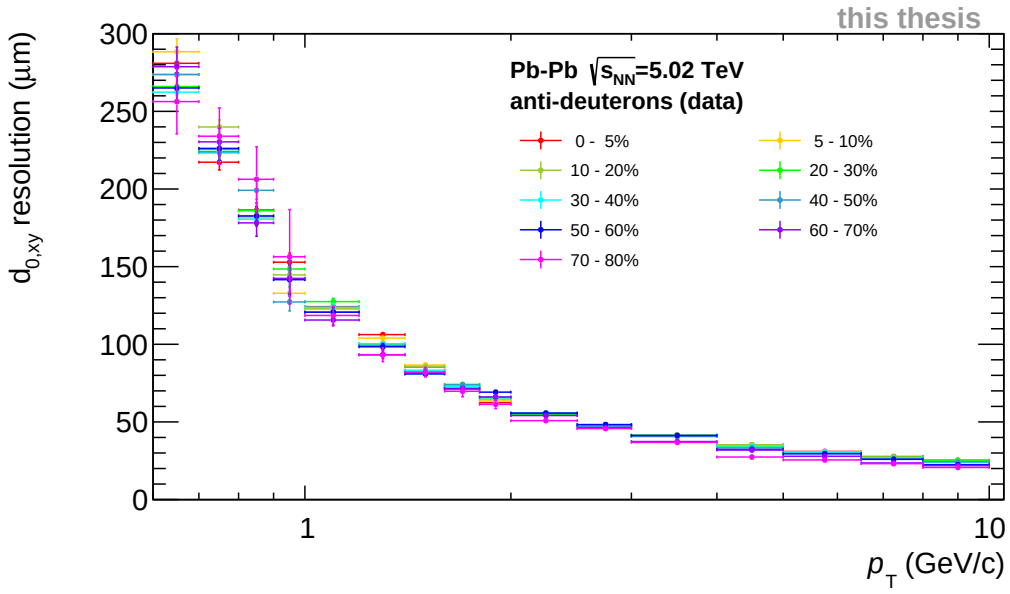

Figure 5.4.: DCA$_{xy}$ resolution vs. transverse momentum p_{T} for different centrality ranges from 0-90% for anti-deuterons. No significant dependence is visible.

To investigate the behavior of the resolution, data was taken for centrality ranges from 0-90% and the procedure of the resolution determination stated in the previous section was applied to this data. The results are depicted in Figure 5.4 for the DCA$_{xy}$ resolution. For the DCA$_z$ resolution similar results were obtained, they are given in the appendix (Figure A.2), as they do not contain any further information. It is evident, that the centrality dependence of the resolution is not significant, as the graphs for different centralities overlap within their uncertainties. But the data for more peripheral events tends to have a slightly better resolution. The reason for this could not be clarified. However, this effect is rather small and this centrality dependence can be seen as negligibly small. So, in conclusion, no significant centrality dependence of the resolution was found. The same results were obtained for the Monte Carlo simulations, they are given in the appendix (see Figure A.3 and Figure A.4).

In addition, the obtained results for the resolution can be compared to previous results for resolution studies of charged particles at $\sqrt{s_{\mathrm{NN}}} = 2.76\,\mathrm{TeV}$. Unfortunately, no previous studies for the

resolution of anti-deuterons or charged particles in Pb-Pb collisions at $\sqrt{s_{\mathrm{NN}}} = 5.02\,\mathrm{TeV}$ exist, so that this comparison is only valid to a limited extent and only the general behavior can be described. In Figure 5.5, the resolutions are depicted for different particle species in pp-collisions and of charged particles in general for different collision systems. Furthermore, the resolution for anti-deuterons is given for comparison.

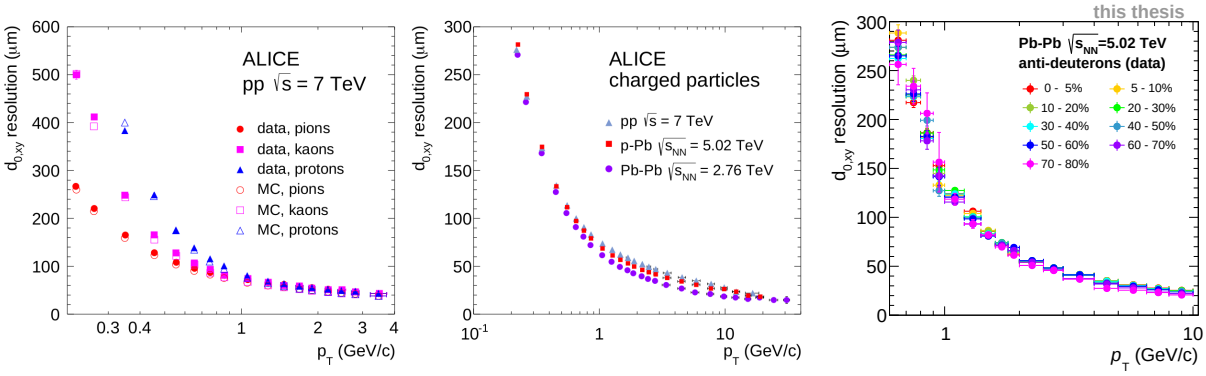

(a) resolution from previous work [4]

(b) this thesis

Figure 5.5.: DCA$_{xy}$ resolution vs. transverse momentum p_{T} for different particle species in pp-collisions (left) and for charged particles in pp, p-Pb and Pb-Pb collisions (middle). Taken from [4]. On the right, the resolution of anti-deuterons is depicted.

It is evident, that the measured resolutions for anti-deuterons are similar to the charged particles resolutions in the higher p_{T} regime (above 2GeV/c) and are worse in the lower transverse momentum region. For example, at 10 GeV/c the resolutions are nearly the same with about 20 μm[1], whereas at about 1 GeV/c, the resolution of anti-deuterons ($\sim$120 μm) nearly doubles the resolution of charged particles ($\sim$70 μm). This can be partly explained by the higher mass of anti-deuterons in comparison to lighter particles like pions, kaons and protons which dominate the charged particles. For heavier particles, the detector resolution is worse and therefore their DCA resolution, too. This effect is also visible for pp-collisions in the left plot of Figure 5.5, where the resolution is given for different particle species. As deuterons are heavier than protons, the graph of their resolution would be above the graph for protons. However, the magnitude of this effect for the anti-deuterons is large, as for a transverse momentum of 1 GeV/c, the resolutions for the different species seem to be rather similar in Figure 5.5.

[1] Since the resolution differences between the different colliding systems are small, Pb-Pb collisions at $\sqrt{s_{\mathrm{NN}}} = 5.02\,\mathrm{TeV}$ are assumed to have similar resolutions.

6. Fraction of primary deuterons

One main goal of this thesis is the determination of the fraction of primary deuterons and complementary to this the fraction of particles produced by the spallation process. This will be carried out in this chapter, as it is essential for understanding the different production processes. To determine the fraction of primary deuterons, a fitting procedure using Monte Carlo simulations will be introduced and improved in the following sections. The procedure will be applied for various momentum and centrality ranges since the fraction is dependent on these variables.

6.1. Fitting procedure

The fraction of primary deuterons can be determined by taking advantage of the differences in the DCA distributions of primary and secondary particles. Whereas the distribution for the primary particles only consists of a narrow peak at a DCA of zero as already mentioned and explained in the last chapter, the secondary particles produced in the detector material have a flat DCA distribution in the first order. This is mainly due to the more isotropically production in the spallation process. The two different DCA distributions for primary and secondary deuterons from material are depicted in Figure 6.1. The distribution for secondary deuterons is mostly flat, but at a DCA of zero, a peak is visible. This peak is caused by secondary tracks, which were wrongly assigned to hits in the ITS, that belong to tracks of primary particles. If a track of a secondary particle is wrongly extrapolated to the SPD cluster of a primary particle, it will directly point to the primary vertex and thus obtain a DCA of zero. In order to determine the fraction of primary particles a histogram fit is carried out, in which the weighted sum of templates for primary and secondary deuterons from material are fitted to the DCA distribution of deuterons. These histogram templates for primary and secondary deuterons are taken from Monte Carlo production. A deuteron contribution that was not taken into account here is the decay of hypertriton since it represents a negligible fraction of the observed deuterons ($\sim$0.03%). However, it will be taken into account in section 6.3 in order to discuss further improvements of the fitting procedure. The fit itself was performed using the TFractionFitter class provided by the ROOT framework since it was built for fitting experimental data with Monte Carlo templates. It takes into account both data and Monte Carlo statistical uncertainties. The fit is a standard likelihood fit using Poisson statistics. The Monte Carlo templates are also varied within statistical uncertainties, leading to additional contributions to the overall likelihood, which results in many more fit parameters. This variation is potentially dangerous, as

the shape of the templates could be varied too much if the statistical uncertainties are too large. In order to avoid this, the used Monte Carlo templates were properly checked to ensure a good quality of the fit. Furthermore, all used histograms were rebinned to minimize the statistical uncertainties. The bin size was increased for larger values of the DCA, since the distribution is rather flat and all information is retained. For the region around the peak for the primary particles a narrower binning was applied to resolve the DCA distribution of the primary deuterons. Lastly, the histogram bins were normalized by their bin widths. The fit was performed in a DCA region from -1 to 1 cm, wider than the actual range which is used for the determination of the fraction of primary deuterons in order to better constrain the fit of the secondary component. After the fit is carried out, the fitter class provides adjusted Monte Carlo templates as well as the fractions for the particles in the selected region.

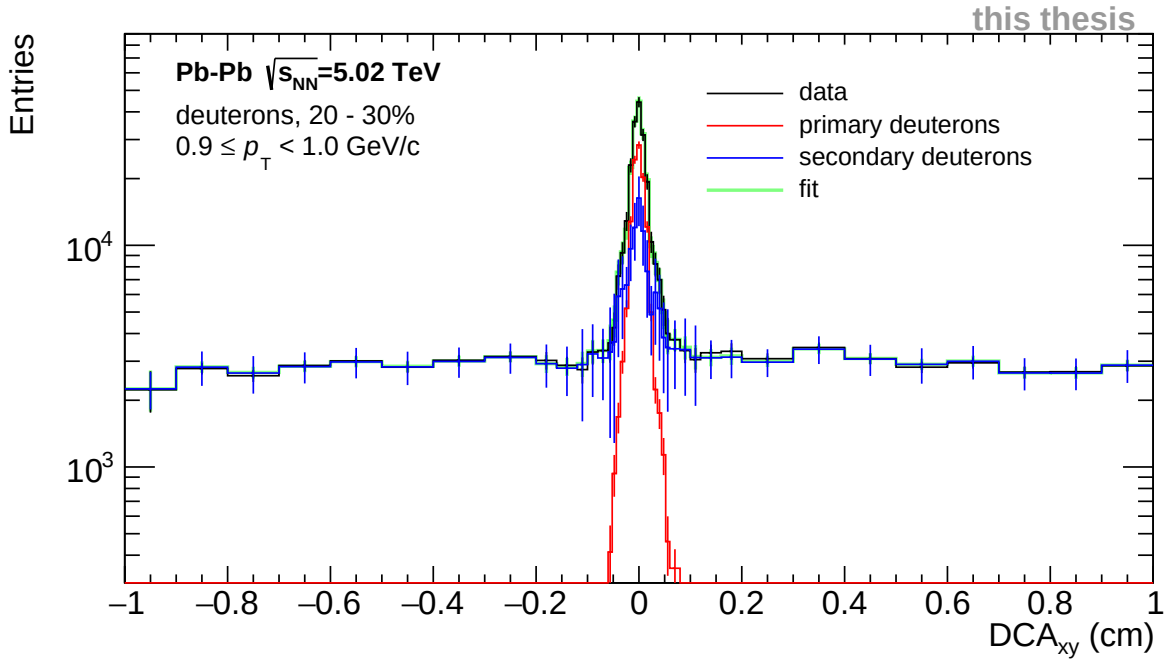

Figure 6.1.: Fit of the DCA$_{xy}$ distribution of deuterons obtained from data (black) with MC templates. The green line represents the sum of the distribution from primary deuterons (red) and secondary deuterons from material (blue).

In order to determine the fraction of primary deuterons, at first, it has to be clarified how it is defined. In recent works [17] the fraction was calculated by integrating the adjusted Monte Carlo templates obtained in the fit in the region from -0.1 cm to 0.1 cm. But this is not accurate, since the resolution of primary deuterons changes for different momenta, so the fraction varies, too. A better approach to this is a fraction calculation that is based on the parametrized resolution for the primary particles. This was carried out here. At first, the resolution and the mean DCA of the primary deuterons are obtained by a Gaussian fit to the adjusted Monte Carlo template with the same procedure as in the previous chapter. Then a range is selected from -3σ to 3σ around the mean

DCA for the primary deuterons, where σ is the resolution.[1] Within this range, the particle yields for primary and secondary particles from material are calculated by integrating the fitted Monte Carlo templates in this region. Following Equation 6.1, the fraction of primary deuterons (f) can be easily calculated using the number of primary particles (n_{p}) and the number of secondary particles from material ($n_{\mathrm{s,M}}$) obtained from the fit:

$$f = \frac{n_{\mathrm{p}}}{n_{\mathrm{p}} + n_{\mathrm{s,M}}} \tag{6.1}$$

The reasons for choosing the fitted Monte Carlo template for the resolution determination rather than the studied resolutions of anti-deuterons in the last chapter is that the resolutions in both of these templates agree within their uncertainties, as confirmed in section 5.3. Also, the uncertainty of the fraction of primary deuterons has to be calculated with special care, since the variables of n_{p} and $n_{\mathrm{s,M}}$ are correlated. For the uncertainties of n_{p} and $n_{\mathrm{s,M}}$ three different uncertainty sources have to be taken into account. First of all, the uncertainty of the fraction determined by the fitter ($\Delta frac_i$), secondly, the uncertainty of the integral of the templates (ΔInt_i) in the selected range and lastly, the uncertainties of the 3σ range of the resolution. The latter uncertainty source will be neglected since it cannot be included properly in the algorithm. The range, that is selected in the histograms can only be varied with at minimum one bin, but since the uncertainty of the resolution is only about 10% of the bin width, a variation of the selected bin range by one bin would overestimate the uncertainty by a factor of ten. For the overall uncertainty of the yields of primary (secondary) deuterons the two left uncertainties are added in quadrature:

$$\frac{\Delta n_i}{n_i} = \sqrt{\left(\frac{\Delta Int_i}{Int_i}\right)^2 + \left(\frac{\Delta frac_i}{frac_i}\right)^2} \tag{6.2}$$

With this in mind the overall uncertainty of the fraction of primary deuterons was calculated as follows:

$$\Delta f = \frac{\partial}{\partial n_{\mathrm{p}}}\left(\frac{n_{\mathrm{p}}}{n_{\mathrm{p}} + n_{\mathrm{s,M}}}\right)\Delta n_{\mathrm{p}} + \frac{\partial}{\partial n_{\mathrm{s,M}}}\left(\frac{n_{\mathrm{p}}}{n_{\mathrm{p}} + n_{\mathrm{s,M}}}\right)\Delta n_{\mathrm{s,M}} \tag{6.3}$$

The fitting procedure was carried out for different p_{T} ranges between 0.6 and 1.6 GeV/c and in various centrality percentiles from 0 to 90% for the DCA$_{xy}$ and the DCA$_z$. The uncertainty for the transverse momentum is directly given by the chosen momentum range. The results of the calculations are given in Figure 6.2 and Figure 6.3.

[1] Note: This selection is only done in the considered DCA, so either the DCA$_{xy}$ or the DCA$_z$. No selection is applied for the other component.

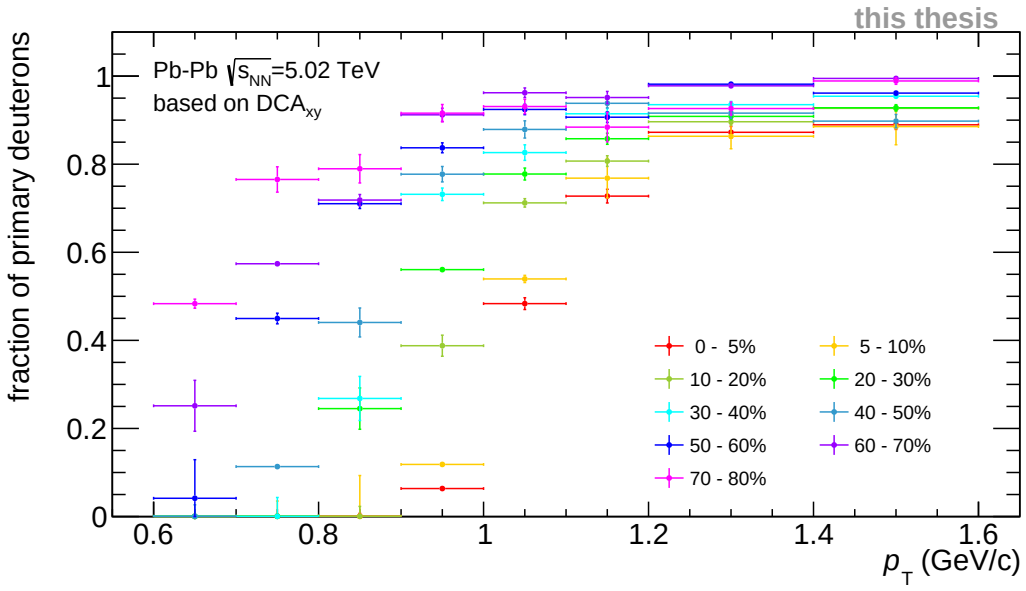

Figure 6.2.: Primary fraction of selected deuterons as a function of the transverse momentum determined using the DCA$_{xy}$. The color characterizes different centrality percentiles.

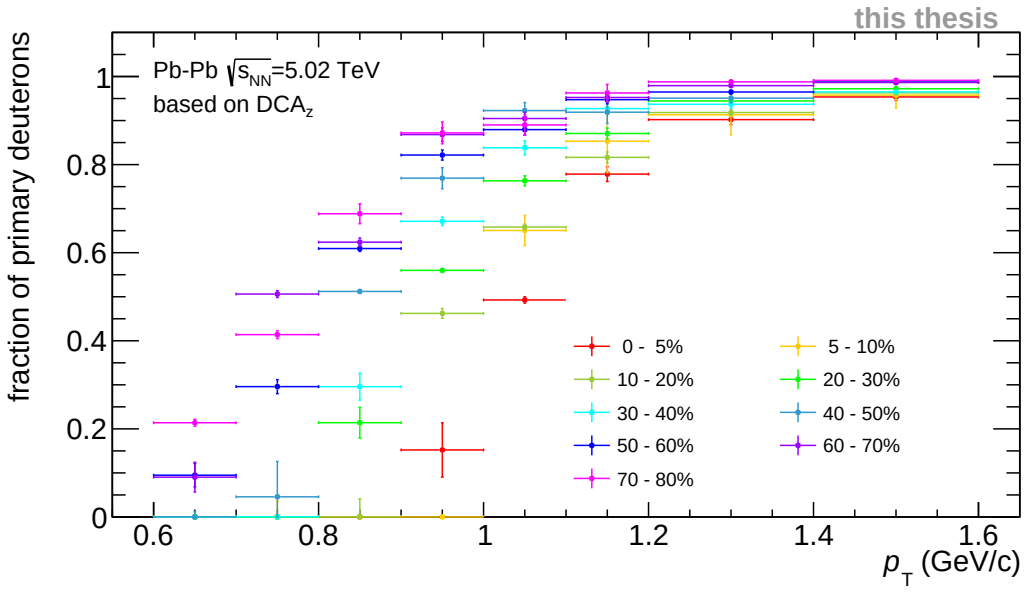

Figure 6.3.: Primary fraction of selected deuterons as a function of the transverse momentum determined using the DCA$_z$. The color characterizes different centrality percentiles.

In these plots two effects are visible. Firstly, the fraction of primary deuterons is dependent on the transverse momentum as expected from the momentum distributions of secondary deuterons from material (see Figure 4.10). The fractions start at low momenta of 0.6-0.7 GeV/c with low fractions of primary deuterons of 0-20%, then the fractions increase rapidly until 1.1-1.2 GeV/c, before they converge towards one. For momenta between 1.4 and 1.6 GeV/c, the fraction of primary deuterons

is for all centralities above 95% due to the fact, that in this region only very few secondary particles occur. Secondly, the fraction of primary deuterons is dependent on the centrality. More peripheral events are connected to a higher fraction and the differences are larger for lower momenta. This can be understood by the consideration of the higher flux of particles in central events. As a result, more secondary particles are produced within the detector material and because of the non-linear behavior of the spallation production process with respect to the multiplicity, the fraction of primary particles decreases. Differences between the fraction of primary deuterons based on the DCA_{xy} and on the DCA_z are mainly due to the different ranges that are selected for the fraction calculations. Two different contradicting effects occur in this context. On the one side, the track selection criteria for the DCA_z are chosen looser ($|\,\mathrm{DCA}_z| \leq 3.2\,\mathrm{cm}$) than for the DCA_{xy} ($|\,\mathrm{DCA}_{xy}| \leq 2.4\,\mathrm{cm}$), therefore more secondary deuterons are taken into account when projecting to the DCA_{xy}. But on the other side, the resolution of the DCA_z is worse, therefore the range for the calculation of the fraction of primary deuterons is larger and more secondary particles are taken into account. The interplay between these two effects was not fully clarified.
The biggest problem with the introduced fitting procedure is, that it fully relies on the accuracy of the Monte Carlo templates because their distributions are taken as the "truth" and they are fitted to the data. However, this assumption is expected to be not fully correct, since the productions process for example for spallation are not yet accurately implemented in GEANT, but it is at the moment the best method to determine the fraction of primary particles.

6.2. Fraction of primary deuterons as a function of multiplicity

With the fitting procedure introduced in the last chapter occurs one problem. For a reasonable fit large Monte Carlo samples are needed in order to minimize the statistical uncertainties. This is especially important because of the variation of the templates by the fitter. However, the number of entries in the histograms decreases rapidly for more peripheral events. Therefore, a good fit cannot be guaranteed, so the fractions for the most peripheral events (80-90%) were not calculated in the last section. However, in order to determine them, the fractions obtained in the previous section for the DCA_{xy} are plotted in Figure 6.4 as a function of the multiplicity, which is directly connected to the centrality. The information about the multiplicity according to the centrality classes was taken from [18], where the multiplicities were measured for different centrality classes in a range of $|\eta| < 0.5$. The results were corrected for acceptance and efficiency. Figure 6.4 contains in principle the same information as Figure 6.2, but displayed differently: The fractions of primary deuterons decrease with higher centrality (higher multiplicity) and the fractions are larger for the lower momentum region. The reasons for these effects were already discussed in the previous section. Unfortunately, an extrapolation to low multiplicities (peripheral events) is not feasible, since the shape of the graphs cannot be described easily with a fitting model. To achieve better results to maybe be able to extrapolate the graphs, more measurement points are needed. However, this decreases the data for the Monte Carlo samples and increases their statistical uncertainties, which leads to less reliable results. The only way to solve these problems is to use larger Monte Carlo samples.

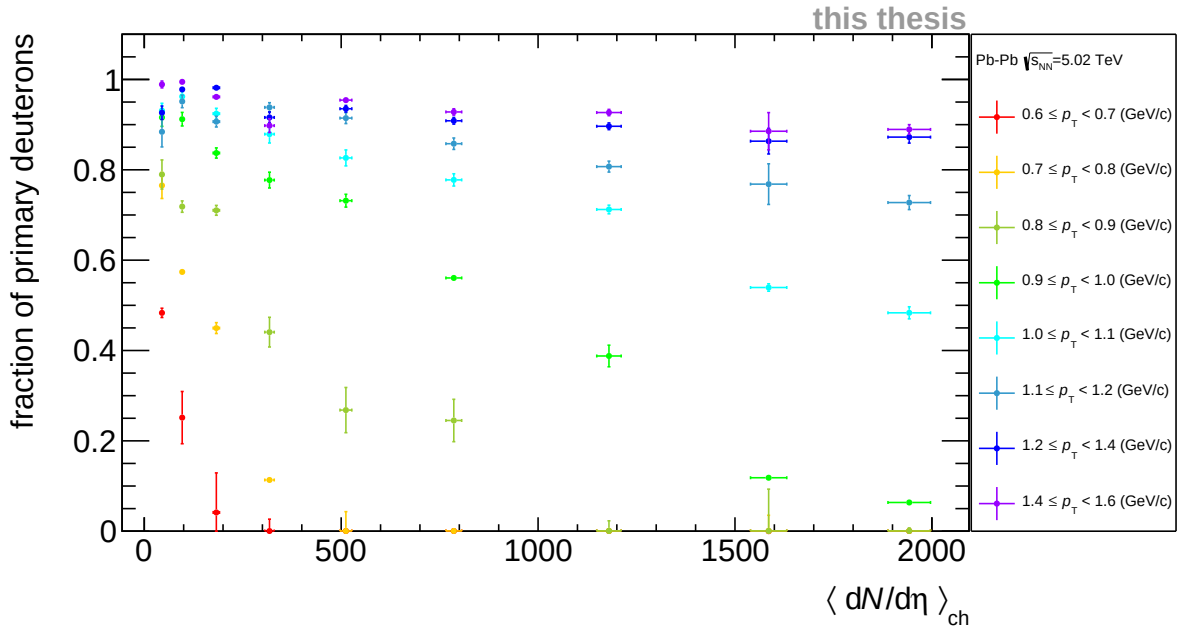

Figure 6.4.: Fraction of primary deuterons as a function of the charged particle multiplicity for different p_{T} ranges (color-coded).

6.3. Fitting procedure with decay deuterons

In order to check the behavior of the fitting procedure, the deuterons that are produced in the decay of the hyper-triton will be taken into account for the fit in this section. Their contribution to the deuterons was seen negligible in the last section, nevertheless considering them might lead to a higher quality of the fits. Therefore, an additional Monte Carlo template for the deuterons produced in the decay processes is fed into the fitting algorithm and the results are compared to the previous ones without the decay deuterons. This can be done since decay deuterons have a broader DCA distribution than primary ones. Figure 6.5 depicts the fit with an additional template of decay deuterons. Since a new source of particles is taken into account, also the fraction determination needs to be adjusted. This can be done easily because the secondary particles from decay can be dealt with analytically in the same way as secondary particles from material. The fraction is now defined with the additional component of secondary decay deuterons $n_{\mathrm{s,D}}$:

$$f_{\mathrm{D}} = \frac{n_{\mathrm{p}}}{n_{\mathrm{p}} + n_{\mathrm{s,M}} + n_{\mathrm{s,D}}}, \tag{6.4}$$

and the uncertainty of the deuteron yield for decay can be calculated according to Equation 6.2, leading to an overall uncertainty for the fraction of:

$$\begin{aligned} \Delta f_{\mathrm{D}} = &\frac{\partial}{\partial n_{\mathrm{p}}} \left(\frac{n_{\mathrm{p}}}{n_{\mathrm{p}} + n_{\mathrm{s,M}} + n_{\mathrm{s,D}}} \right) \Delta n_{\mathrm{p}} + \frac{\partial}{\partial n_{\mathrm{s,M}}} \left(\frac{n_{\mathrm{p}}}{n_{\mathrm{p}} + n_{\mathrm{s,M}} + n_{\mathrm{s,D}}} \right) \Delta n_{\mathrm{s,M}} \\ &+ \frac{\partial}{\partial n_{\mathrm{s,D}}} \left(\frac{n_{\mathrm{p}}}{n_{\mathrm{p}} + n_{\mathrm{s,M}} + n_{\mathrm{s,D}}} \right) \Delta n_{\mathrm{s,D}} \end{aligned} \tag{6.5}$$

In Figure 6.5, an example for the fraction fit is shown. It is visible, that the shapes for the DCA distributions of the three production processes differ. Moreover, the fraction of decay deuterons is small in comparison to the other components, as expected.

To validate the results obtained, the expected yield of the decay deuterons can be estimated with the general yields of deuterons and hyper-tritons as well as the branching ratio for the decay of hyper-triton to deuterons and the reconstruction efficiency:

$$\text{ratio of decay particles} = \frac{\left(\frac{\mathrm{d}N}{\mathrm{d}y}\right)_{^3_\Lambda\mathrm{H}} \cdot \text{BR(3-body decay)} \cdot \epsilon_{\mathrm{rec}}}{\left(\frac{\mathrm{d}N}{\mathrm{d}y}\right)_{\mathrm{d}}} \tag{6.6}$$

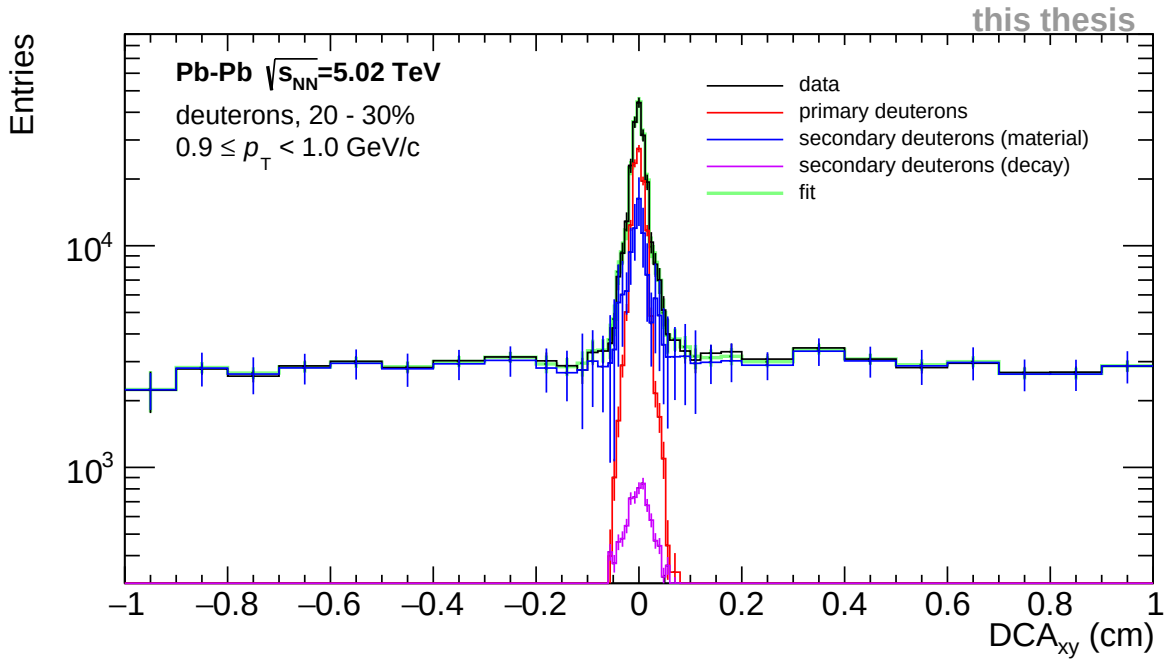

Figure 6.5.: Fit of the DCA$_{xy}$ distribution of deuterons to the data (black). The green line represents the sum of the distribution from primary deuterons (red) and secondary deuterons from material (blue) and from decay (violet).

The branching ratio for the three-body decay for the hyper-triton is 41%. The yield $\left(\frac{\mathrm{d}N}{\mathrm{d}y}\right)_{^3_\Lambda\mathrm{H}}$ of the hypertriton was taken from [19] for the most central events from 0-10% centrality, it is integrated over the whole momentum range. The yield for the deuterons $\left(\frac{\mathrm{d}N}{\mathrm{d}y}\right)_{\mathrm{d}}$ was taken from [17] for a centrality of 0-5%, it is integrated over the whole momentum range, too. Furthermore, the yields are corrected for efficiency and acceptance. The reconstruction efficiency ϵ_{rec} characterizes the different efficiencies for the detection of primary and decay deuterons. The efficiency for the detection of decay deuterons is smaller than for primary deuterons since some tracks of these particles are excluded by the track selection. The reconstruction efficiency was estimated to ϵ_{rec} =0.6. With Equation 6.6, the maximum fraction between decay deuterons and primary deuterons was estimated roughly to be within the magnitude of 0.03%. The value obtained from the fit, which is shown in Figure 6.5, was in comparison (8.75 $\pm$ 0.21)%, which is significantly differing by two orders of magnitude. Nevertheless, further fits were performed and the fractions of primary deuterons were calculated again. The results of the fraction determination are depicted in Figure 6.6. It is evident, that the determined fractions have larger uncertainties and especially in the low transverse momentum range, the fractions differ significantly from the previously determined ones. The reason for this becomes clear when the fraction between secondary particles from decay processes and primary particles is also formed. In low momentum ranges this fraction increases up to 60%, meaning the fitter is not able to distinguish primary deuterons and secondary decay deuterons because of the rather small peak in the DCA distribution. This leads to systematically

wrong fractions since the fraction of decay deuterons is expected to be about 0.03%. For higher momentum ranges, the fits are better, the fraction of decay deuterons here is at about a few percents. In order to check if the fits obtained a higher quality, the χ^2 per Number Degrees of Freedom were calculated for the fitting procedure without and with the additional template for decay deuterons. The distributions of the χ^2/NDF are shown in Figure 6.7. It is visible, that the additional template does not improve the fit since the distributions are similar. In summary, a consideration of the decay particles does not lead to any improvement, but even worsens the result, because especially for low momenta the templates for primary deuterons and secondary decay deuterons processes cannot be distinguished by the Fitter. Including decay deuterons requires much higher precision to be of advantage due to the very low expected yield of secondary decay deuterons (about 0.03%). The fit without decay particles is, therefore, a much more appropriate attempt, which is sufficiently good.

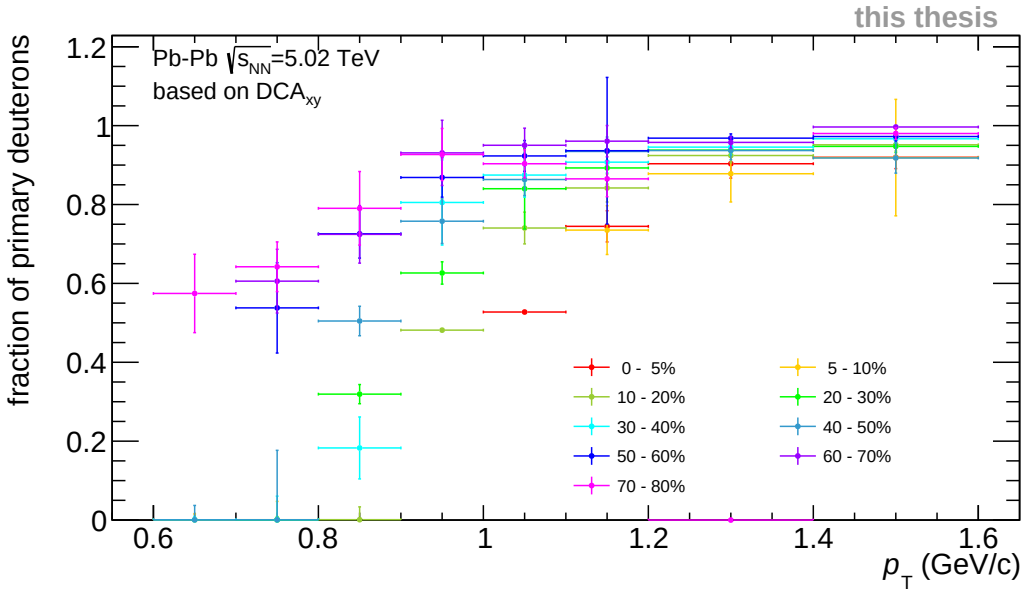

Figure 6.6.: Primary fraction of selected deuterons as a function of the transverse momentum determined using the DCA$_{xy}$ with an additional template for decay deuterons. The color characterizes different centrality percentiles.

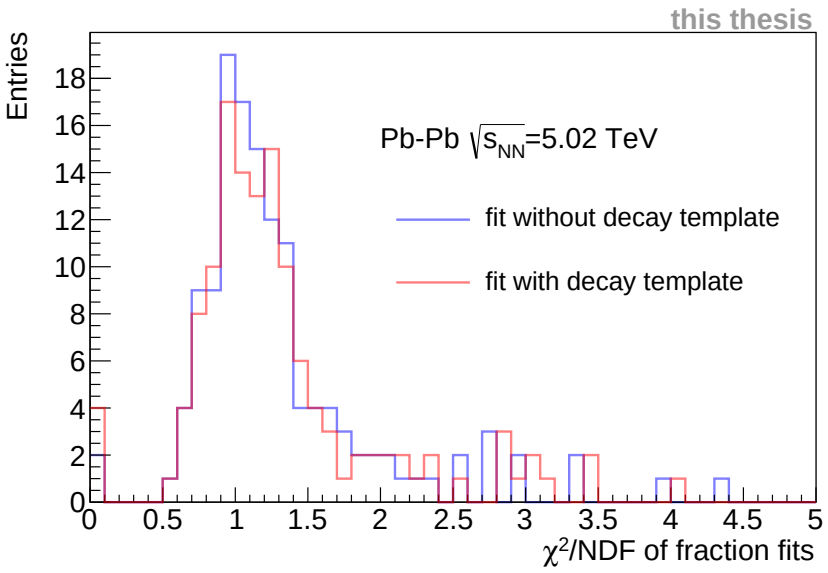

Figure 6.7.: χ^2 per Number Degrees of Freedom for the performed fits for the determination of the fraction of primary deuterons with and without an additional deuteron decay template.

6.4. 2D-fit

The fitting procedure introduced in the last sections is based only on one component of the DCA, either the DCA_{xy} or the DCA_z. Any information according to the other component is not used during the fit and gets lost in the projection to one component. To fully use the information provided by both components, the possibility of a two dimensional fit will be briefly discussed in this section. In principle, a two-dimensional fit with respect to both DCA components would be the most accurate way to determine the fraction of primary deuterons, since the full correlation between the components is used. An example for the DCA distribution for deuterons is depicted in Figure 6.8 (right). Visible are the contributions of secondary deuterons from material, which form the green background, and from primary deuterons originating from the primary vertex at a DCA of zero, which form the red ellipse in the middle. This elliptical shape of the distribution of primary particles has its origin in the different resolutions of the DCA components. With this in mind, the region, in which the number of primary particles is calculated, has to be elliptical with $3\sigma_{xy}$ as the semi-minor axis and $3\sigma_z$ as the semi-major axis. The left and the middle panel of Figure 6.8 show examples of the DCA distributions for primary and secondary deuterons obtained from Monte Carlo simulations, the sample for primaries with one clear peak at zero and the sample for secondary particles with a more flat distribution.

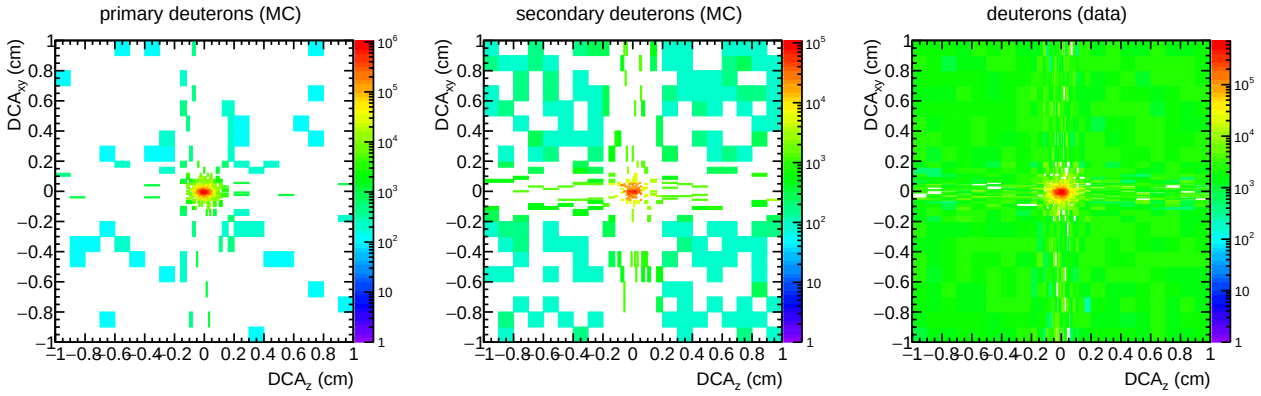

Figure 6.8.: Two dimensional distribution of the DCA for the Monte Carlo template of primary deuterons (left), of secondary deuterons from material (middle) and the DCA distribution of deuterons obtained from data. Centrality range: 0-5%, transverse momentum range: 1.0-1.1 GeV/c.

Unfortunately, the Monte Carlo sample for the secondary deuterons consists of a lot of empty bins in the regions of larger DCAs as a result of a low number of entries, which heavily influences the quality of the fraction fit. Nevertheless, an attempt was made to carry out the fit for the determination of the fraction of primary particles. This was done similarly as before, albeit now with two-dimensional histograms. But as expected, the fitter was not able to fit the Monte Carlo samples to the data because of the low number of entries for the secondary deuterons from material. Even if the fitter would have been able to fit the data, the results were not reliable, since the low number of entries imply large statistical uncertainties, which could lead to dangerous adjustments and variations of the templates. Therefore, this procedure of a two-dimensional fit is only feasible, if Monte Carlo samples with large enough statistics can be used.

7. Summary and outlook

The aim of this thesis was the investigation of the spallation process. In this context, three major topics were examined in detail. In the first part, possible additional selection criteria for better discrimination of primary and secondary deuterons were investigated. For this, the selection of (anti-)deuterons and the separation into primary and secondary particles were described first. (Anti-)Deuterons were selected with the particle identification information provided by the ITS, the TPC and the TOF detector. They passed the selection, if their PID signal differed less than n times the detector resolution (σ) from the expected signal. For the ITS, n ranged from -3 to 4, for the TPC from -3 to 3 and for the TOF detector from -3 to 3, only for momenta above 0.9 GeV/c. The additional TOF selection was carried out since the ITS and TPC do not provide a clear separation of particles in the higher momentum regime. Primary and secondary deuteron samples were created by a DCA selection. These samples were used to investigate further variables regarding the discrimination between primary and secondary deuterons. It was found, that the requirement of a hit in the first ITS layer reduces the number of secondary particles by 44% in comparison to the requirement of at least one hit in any of the SPD layers while losing 13% of the primary deuterons. Furthermore, a requirement of no shared cluster in the first SPD layer reduces the number of secondary deuterons that have a hit in this layer by 20% while the number of primaries is reduced by 8.5%. Therefore, additional requirements to the ITS may improve the separation between primary and secondary particles. Variables that were not useful in this context were the dE/dx-η distribution as well as the χ^2/NDF distributions for the ITS and TPC. As the χ^2/NDF is a variable that describes the quality of the track in the ITS and the TPC, respectively, it was expected that it is worse for secondaries since they mostly lack of hits in the ITS. However, this could not be verified and no major difference was found. In the second part, the DCA resolution of anti-deuterons as a proxy for primary deuterons was investigated. This was done for different SPD requirements and it was found, that looser requirements are connected to worse resolutions as expected. Moreover, the centrality dependence and the differences to Monte-Carlo simulations were examined. No significant centrality difference was found and a good agreement of data and Monte Carlo simulation was verified in this context. In the third and last part of the analysis, the fraction of primary deuterons in a range of DCA values around zero was investigated and attempts were made to improve the determination. The fraction is commonly determined by a fitting procedure using Monte Carlo templates, which was outlined in chapter 6. So far, the fraction was calculated considering a fixed range in the DCA from -0.1 cm to 0.1 cm. However, since the resolution of primary deuterons is dependent on the transverse momentum (chapter 5), a new method was introduced, based on the

resolution. In detail, the fraction was calculated in a 3σ range around the mean DCA for primary deuterons, where σ is the DCA resolution in the specific momentum range. In this context, the fraction of primary deuterons was also studied as a function of the event multiplicity in order to extrapolate the fractions to lower multiplicities, but this was not possible accurately. For further improvements of the fitting procedure the deuterons produced in weak decay processes were taken into account and the possibility of a two-dimensional fit was discussed. However, the consideration of the decay deuterons did not lead to any improvement, since the yield of deuterons from decay is too small to be considered properly in the fit (0.03%). A two-dimensional fit is not possible yet since the Monte Carlo samples are not large enough at the moment, but this could be fixed in the future.
The next steps to extend these studies of the spallation process would be the following ones:

- Obtain larger Monte Carlo samples to be able to apply a two-dimensional fit
- Extend the analysis to other particles that are produced via the spallation process like for example ^{3}He
- Use more advanced methods like machine learning to investigate further discrimination variables
- Do a systematic characterization of the spallation process

This could be used to improve the description of secondary particles from material in the Monte Carlo simulation. Results of this and following works may lead to an adjustment of the implementation of them in GEANT, which also would improve the determination of the fraction of primary particles since the precision of the Monte Carlo description has a significant impact on the precision of the fraction determination. These results would be of crucial importance for understanding the production processes of particles in collisions and beyond.

List of abbreviations

ALICE A Large Ion Collider Experiment
LHC Large Hadron Collider
ITS Inner Tracking System
TPC Time Projection Chamber
TRD Transition Radiation Detector
TOF Time Of Flight
PHOS Photon Spectrometer
EMCal Electromagnetic Calorimeter
HMPID High Momentum Particle Identification Detector
SPD Silicon Pixel Detector
SDD Silicon Drift Detector
SSD Silicon Strip Detector
PID Particle Identification
QCD Quantum Chromodynamics
IROC inner readout chamber
OROC outer readout chamber
QGP Quark Gluon Plasma
MC Monte Carlo
DCA Distance of Closest Approach

Bibliography

[1] J. Stachel, A. Andronic, P. Braun-Munzinger, and K. Redlich, "Confronting LHC data with the statistical hadronization model", *J. Phys.: Conf. Ser.509 012019*, 2014. DOI: doi:10.1088/1742-6596/509/1/012019.

[2] R. Scheibl and U. W. Heinz, "Coalescence and flow in ultrarelativistic heavy ion collisions", *Phys.399Rev.C59(1999) 1585–1602*, 1999. arXiv: nucl-th/9809092 [nucl-th].

[3] M. L. Miller, K. Reygers, S. J. Sanders, and P. Steinberg, "Glauber Modeling in High Energy Nuclear Collisions", *Ann.Rev.Nucl.Part.Sci.57:205-243*, 2007. arXiv: nucl-ex/0701025 [nucl-ex].

[4] ALICE Collaboration, "Performance of the ALICE Experiment at the CERN LHC", *Int. J. Mod. Phys. A 29 (2014) 1430044*, 2014. arXiv: 1402.4476 [nucl-ex].

[5] M. Puccio, "Study of the production of nuclei and anti-nuclei at the LHC with the ALICE experiment", PhD thesis, Università degli studi di Torino Scuola di Dottorato in Scienze della Natura e Tecnologie Innovative Dipartimento di Fisica, 2017. [Online]. Available: http://inspirehep.net/record/1652942/files/11773-Puccio-dottorato.pdf.

[6] B.Alver, M.Baker, C.Loizides, and P. (BNL), "The PHOBOS Glauber Monte Carlo", 2008. arXiv: arXiv:0805.4411 [nucl-ex].

[7] R. Lea. (2017). Production of light (anti-)nuclei and (anti-)hypernuclei with ALICE at the LHC, [Online]. Available: https://indico.cern.ch/event/656756/attachments/1526030/2394107/CERNSEMINARv3.pdf (visited on 07/24/2019).

[8] A. Krása, "Spallation Reaction Physics", 2010.

[9] C.-M. Herbach, D. Hilscher, U. Jahnke, V. Tishchenko, J. Galin, A. Letourneau, A. Péghaire, D. Filges, F. Goldenbaum, L. Pienkowski, W. Schröder, and J. Tõke, "Charged-particle evaporation and pre-equilibrium emission in 1.2 GeV proton-induced spallation reactions", *Nuclear Physics A 765 (2006) 426–463*, 2005. DOI: 10.1016/j.nuclphysa.2005.10.014.

[10] ALICE Collaboration, "The ALICE Experiment at the CERN LHC", *JINST 3 S08002*, 2008. DOI: 10.1088/1748-0221/3/08/s08002.

[11] L. Betev *et al.*, "Definition of the ALICE coordinate system and basic rules for sub-detector components numbering", *ALICE-INT-2003-038*, 2003. [Online]. Available: http://edms.cern.ch/document/406391.

[12] ALICE Collaboration, “ALICE time projection chamber: Technical Design Report”, *CERN-LHCC-2000-012*, 2000. [Online]. Available: http://cdsweb.cern.ch/record/451098.

[13] ALICE Collaboration, “Technical Design Report for the Upgrade of the ALICE Time Projection Chamber”, *CERN-LHCC-2015-002*, 2014. [Online]. Available: https://cds.cern.ch/record/1622286/files/ALICE-TDR-016.pdf.

[14] ALICE Collaboration. (2019). The ALICE Time of Flight Detector, [Online]. Available: http://aliceinfo.cern.ch/Public/en/Chapter2/Chap2_TOF.html (visited on 05/07/2019).

[15] B. Batyunya, Y. Belikov, and K. Šafařík, “Kalman Filtering application for track recognition and reconstruction in ALICE tracking system”, 1997. [Online]. Available: http://cds.cern.ch/record/689414/files/INT-1997-24.pdf.

[16] S. Agostinelli et al., “Geant4—a simulation toolkit”, *Nuclear Instruments and Methods in Physics Research Section A: Accelerators, Spectrometers, Detectors and Associated Equipment*, vol. 506, no. 3, pp. 250–303, 2003. DOI: 10.1016/S0168-9002(03)01368-8.

[17] M. Puccio, S. Bufalino, and M. Masera, “Analysis note: Nuclei production in Pb–Pb collisions at $\sqrt{s_{NN}} = 5.02$ TeV”, 2012. [Online]. Available: https://alice-notes.web.cern.ch/node/626.

[18] ALICE Collaboration, “Centrality dependence of the charged-particle multiplicity density at mid-rapidity in Pb-Pb collisions at $\sqrt{s_{\mathrm{NN}}} = 5.02$ TeV”, 2015. arXiv: arXiv:1512.06104 [nucl-ex].

[19] S. Trogolo, S. Bufalino, and E. Botta, “Production of ${}^{3}_{\Lambda}\mathrm{H}$ and ${}^{3}_{\Lambda}\bar{\mathrm{H}}$ in Pb–Pb collisions at $\sqrt{s_{NN}} = 5.02$ TeV”, 2018. [Online]. Available: https://alice-notes.web.cern.ch/node/776.

A. Additional results

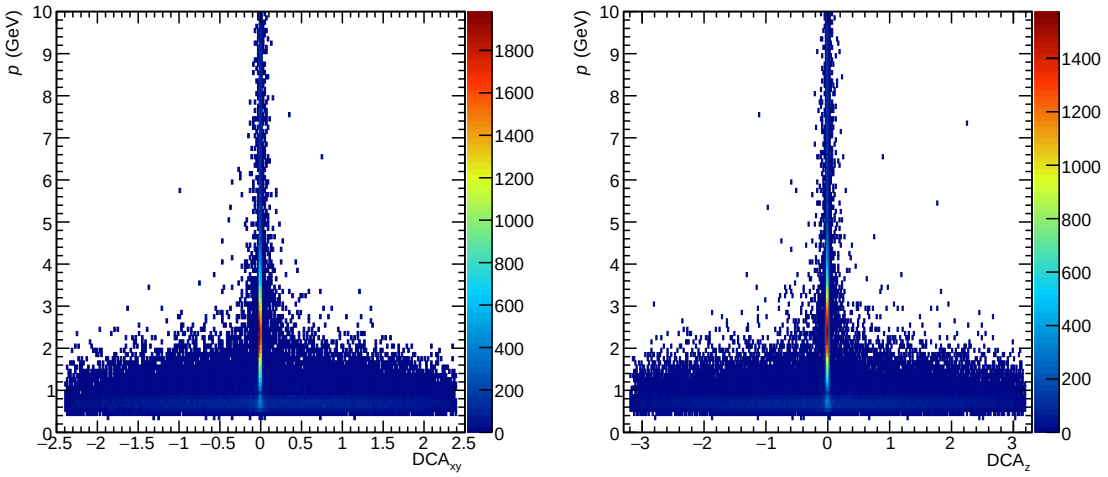

Figure A.1.: Momentum p vs. DCA$_{xy}$ and DCA$_z$ for deuterons. Particles with large DCA values are produced by interaction with the detector material. They do not exceed 3 GeV.

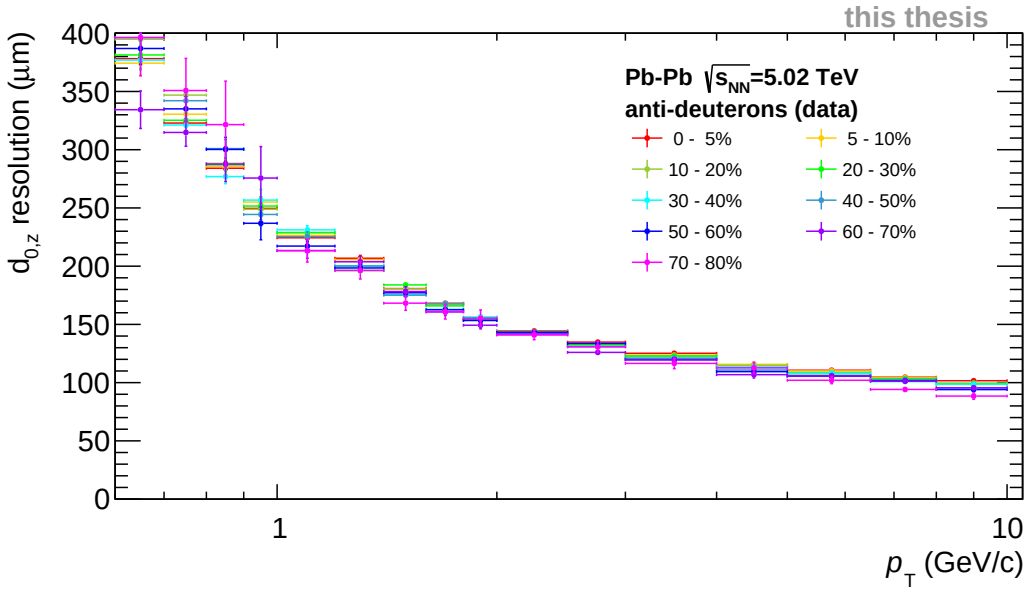

Figure A.2.: DCA$_z$ resolution vs. transverse momentum p_{T} for different centrality ranges from 0-90% for anti-deuterons. No significant dependence is visible.

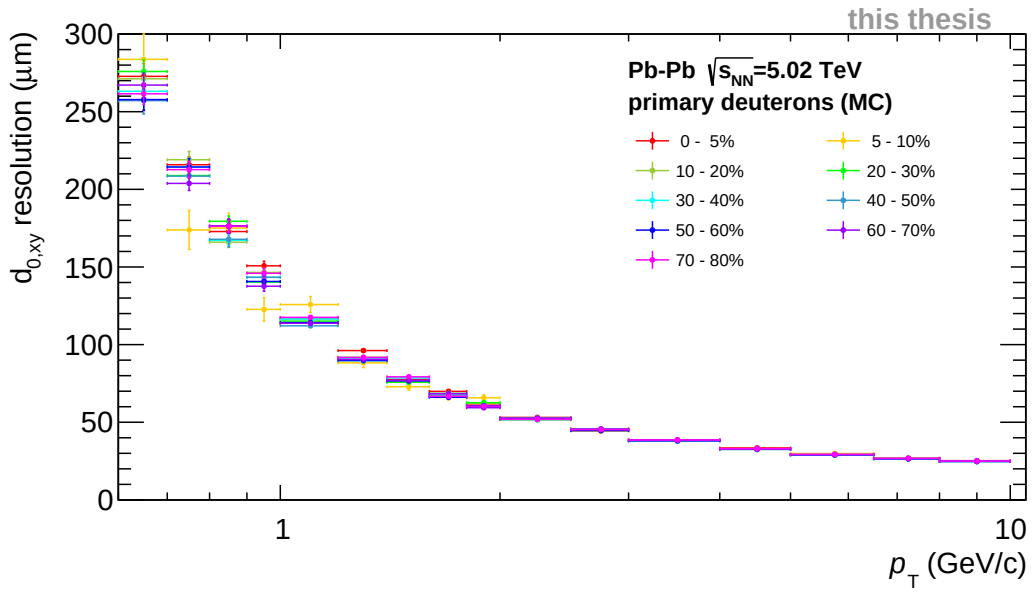

Figure A.3.: DCA$_{xy}$ resolution vs. transverse momentum p_{T} for different centrality ranges from 0-90% for primary deuterons produced in the Monte Carlo simulation.

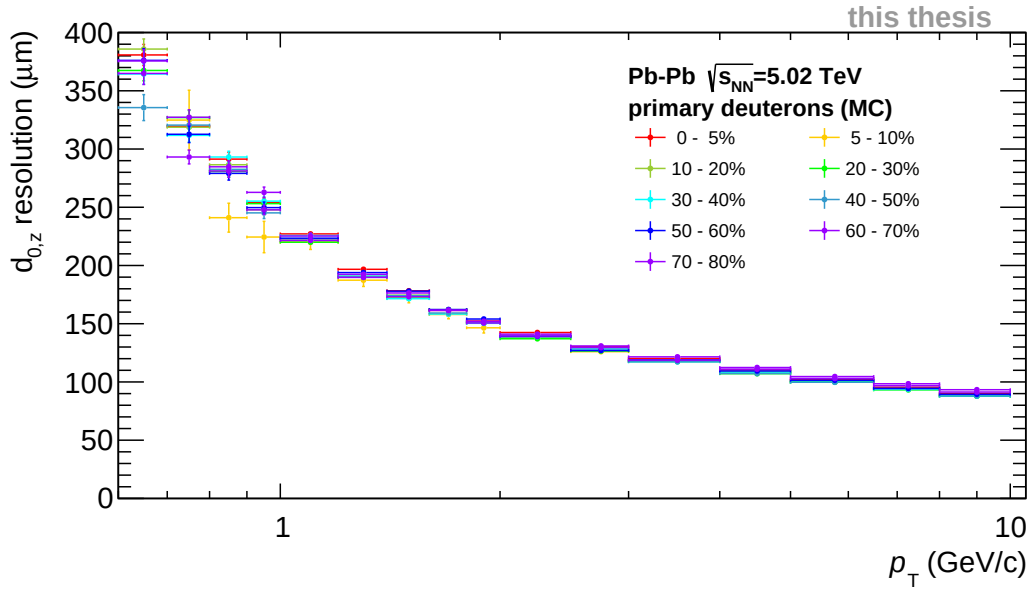

Figure A.4.: DCA$_z$ resolution vs. transverse momentum p_{T} for different centrality ranges from 0-90% for primary deuterons produced in the Monte Carlo simulation.

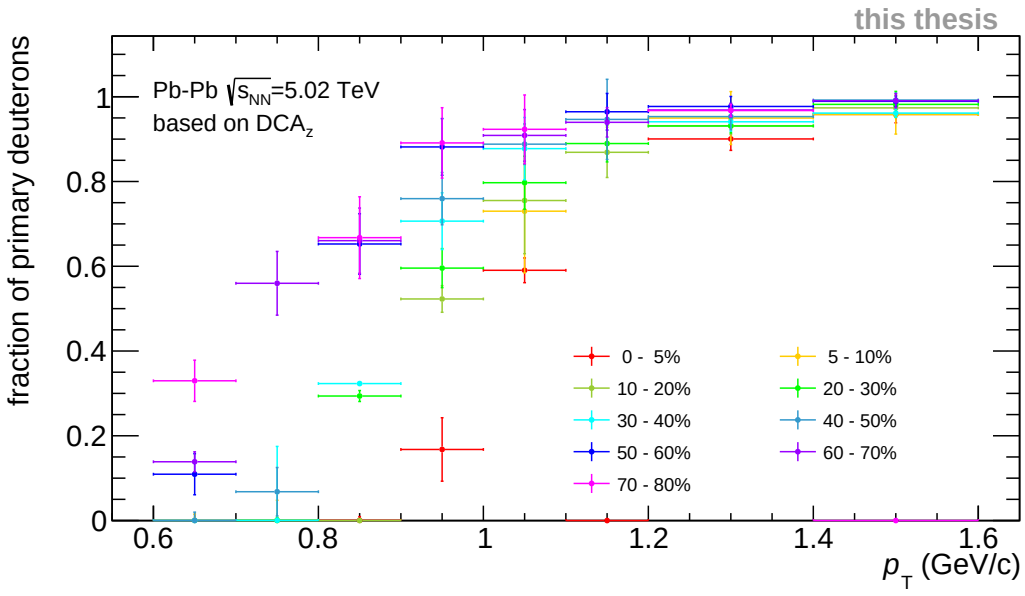

Figure A.5.: Primary fraction of selected deuterons as a function of the transverse momentum determined using the DCA_z with an additional template for decay deuterons. The color characterizes different centrality percentiles.

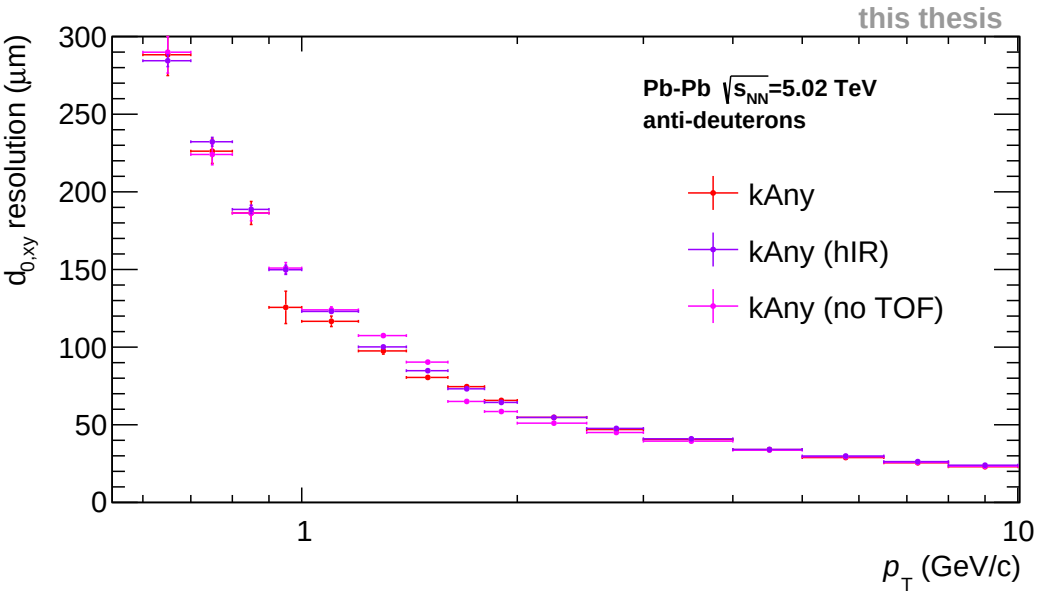

Figure A.6.: Comparison of DCA_{xy} resolution vs. transverse momentum p_{T} for high and low interaction rate runs. No significant difference is visible.

Erklärung

Ich versichere, dass ich diese Arbeit selbstständig verfasst und keine anderen als die angegebenen Quellen und Hilfsmittel benutzt habe.

Heidelberg, den 04.09.2019,